

# Measuring $D_A$ and $H$ at $z = 0.35$ from the SDSS DR7 LRGs using baryon acoustic oscillations

Xiaoying Xu<sup>1</sup>, Antonio J. Cuesta<sup>2</sup>, Nikhil Padmanabhan<sup>2</sup>, Daniel J. Eisenstein<sup>3</sup>, Cameron K. McBride<sup>3</sup>

<sup>1</sup> *Steward Observatory, University of Arizona, 933 N. Cherry Ave., Tucson, AZ 85721; xxu@as.arizona.edu*

<sup>2</sup> *Department of Physics, Yale University, 260 Whitney Ave., New Haven, CT 06511*

<sup>3</sup> *Harvard-Smithsonian Center for Astrophysics, Harvard University, 60 Garden St., Cambridge, MA 02138*

21 March 2022

## ABSTRACT

We present measurements of the angular diameter distance  $D_A(z)$  and the Hubble parameter  $H(z)$  at  $z = 0.35$  using the anisotropy of the baryon acoustic oscillation (BAO) signal measured in the galaxy clustering distribution of the Sloan Digital Sky Survey (SDSS) Data Release 7 (DR7) Luminous Red Galaxies (LRG) sample. Our work is the first to apply density-field reconstruction to an anisotropic analysis of the acoustic peak. Reconstruction partially removes the effects of non-linear evolution and redshift-space distortions in order to sharpen the acoustic signal. We present the theoretical framework behind the anisotropic BAO signal and give a detailed account of the fitting model we use to extract this signal from the data. Our method focuses only on the acoustic peak anisotropy, rather than the more model-dependent anisotropic information from the broadband power. We test the robustness of our analysis methods on 160 LasDamas DR7 mock catalogues and find that our models are unbiased at the  $\sim 0.2\%$  level in measuring the BAO anisotropy. After reconstruction we measure  $D_A(z = 0.35) = 1050 \pm 38$  Mpc and  $H(z = 0.35) = 84.4 \pm 7.0$  km/s/Mpc assuming a sound horizon of  $r_s = 152.76$  Mpc. Note that these measurements are correlated with a correlation coefficient of 0.57. This represents a factor of 1.4 improvement in the error on  $D_A$  relative to the pre-reconstruction case; a factor of 1.2 improvement is seen for  $H$ .

**Key words:** distance scale – cosmological parameters – large-scale structure of universe – cosmology: theory, observations

## 1 INTRODUCTION

One of the major challenges in modern cosmology is to understand cosmic acceleration, a crucial but perplexing discovery made through observations of distant supernovae (Riess et al. 1998; Perlmutter et al. 1999). This expansion is typically attributed to “dark energy” which makes up nearly 75% of the universal energy budget (e.g. Mehta et al. 2012). Despite its ubiquitous nature, our understanding of its physical properties is poor. It is possible to gain leverage on the dark energy equation of state  $w$ , as well as other cosmological parameters such as  $\Omega_K$  through studying the cosmic expansion history. We will use an extension of the baryon acoustic oscillations method, namely its anisotropic signature, to probe cosmic expansion in this paper.

Baryon acoustic oscillations (BAO) arise from the interactions between matter and radiation in the early universe. The story begins with the seeding of primordial overdensities composed of dark matter, baryons, photons

and neutrinos. Prior to recombination, the large density of free electrons locks the photons and baryons together via Thomson scattering. As the overdensities grow gravitationally, they also heat up and the photons become very energetic. The radiation pressure becomes large enough to push the photon-baryon fluid outwards in a spherical soundwave. The dark matter, which remains at the central overdensity, exerts a gravitational restoring force on the fluid. The competition between the outward push by radiation and the inward pull of gravity gives rise to a system of standing sound waves within the plasma (Peebles & Yu 1970; Sunyaev & Zeldovich 1970; Bond & Efstathiou 1984; Holtzman 1989; Hu & Sugiyama 1996; Hu & White 1996; Eisenstein & Hu 1998). The period of these waves corresponds to a characteristic spatial scale known as the acoustic scale or the sound horizon. This scale,  $\sim 150$  comoving Mpc, is the distance traveled by the sound wave in the plasma prior to recombination. When recombination occurs, the free electrons are quickly captured

which ends the coupling between the photons and baryons. The photons stream away, forming the cosmic microwave background (CMB), and the baryons are left behind at characteristic separations corresponding to the acoustic scale. This scale is still measurable in the clustering distribution of galaxies today, which makes it an ideal standard ruler (Eisenstein & Hu 1998; Eisenstein, Hu & Tegmark 1998; Blake & Glazebrook 2003; Eisenstein 2003; Hu & Haiman 2003; Linder 2003; Seo & Eisenstein 2003; Matsubara 2004; Abdalla & Rawlings 2005; Amendola, Quercellini & Giallongo 2005; Angulo et al. 2005; Glazebrook & Blake 2005; Dolney, Jain & Takada 2006). We can use this ruler to measure the distance to various redshifts using the clustering distribution of galaxies measured from large galaxy surveys. This distance-redshift relation depends on the values of the cosmological parameters, including those governing dark energy, so it can be used to infer the cosmic expansion history and the cosmology of the universe.

To use the BAO method, we must first measure the acoustic scale from the clustering of galaxies. This is typically done statistically using the 2-point correlation function of galaxy separations or its Fourier transform, the power spectrum. Past BAO studies have primarily been focused on the spherically-averaged (monopole) statistics (Cole et al. 2005; Eisenstein et al. 2005; Hütsi 2006; Tegmark et al. 2006; Percival et al. 2007; Kazin et al. 2010a; Percival et al. 2010; Beutler et al. 2011; Blake et al. 2011a; Padmanabhan et al. 2012; Xu et al. 2012; Mehta et al. 2012), which only allow us to measure the spherically-averaged distance  $D_V(z) \propto D_A(z)^2/H(z)$ , where  $z$  is the median redshift of the galaxy sample. This effectively assumes that the clustering of galaxies is isotropic. Most importantly, the Hubble parameter  $H(z)$  is degenerate with  $D_A(z)$  in this measure and hence we cannot directly probe the cosmic expansion history encoded by  $H(z)$ .

The clustering of galaxies, however, is not truly isotropic. Anisotropies arise from large-scale redshift-space distortions caused by the line-of-sight velocity of galaxies (Kaiser 1987) and from assuming the wrong cosmology when calculating the 2-point statistics. This second point can be used to break the degeneracy between  $H(z)$  and  $D_A(z)$ . One can imagine that if we assume the wrong cosmology, then the BAO will appear at slightly different locations along the line-of-sight and transverse directions because the line-of-sight distances are measured from redshifts and  $H(z)$ , whereas the transverse distances are measured using the angular separation and  $D_A(z)$ .

The use of such anisotropies to measure the cosmic expansion history was first proposed by Alcock & Paczynski (1979). In the case of the BAO, the anisotropy can be measured using the clustering signal along different directions (Okumura et al. 2008; Gaztañaga, Cabré & Hui 2011; Blake et al. 2011b; Chuang & Wang 2012a; Kazin, Sánchez & Blanton 2012) or by looking at higher order multipoles of the 2-point statistics (Padmanabhan & White 2008; Taruya, Saito & Nishimichi 2011; Chuang & Wang 2012b). If the clustering were isotropic, then all higher order multipoles should be zero. However, anisotropies introduce power into the even multipoles (the odd multipoles remain zero due to symmetry).

This fact can be exploited to infer the values of  $H(z)$  and  $D_A(z)$  (see §2).

In this paper, we will focus on the multipole method and apply the technique described in Padmanabhan & White (2008) to the 7th data release (DR7; Abazajian et al. 2009) of the Sloan Digital Sky Survey (SDSS). We present the first application of this method to a galaxy redshift survey and demonstrate its feasibility. We calibrate our methods on 160 LasDamas mocks and perform detailed tests to ensure their robustness. We also apply reconstruction, a technique for partially removing the effects of non-linear structure growth on the BAO (Eisenstein et al. 2007). This technique has been tested extensively on the monopole through simulations (Seo et al. 2008; Padmanabhan, White & Cohn 2009; Noh, White & Padmanabhan 2009; Seo et al. 2010; Mehta et al. 2011) and has recently been applied to SDSS DR7 data (Padmanabhan et al. 2012; Xu et al. 2012; Mehta et al. 2012). The current work takes a first look at how reconstruction affects the anisotropic BAO signal and uses this to infer  $H(z)$  and  $D_A(z)$  from the DR7 data.

In §2 we present the theoretical background for the multipole method. In §3 we present our analysis techniques with emphasis on the intricacies of the fitting model. In §4 we introduce the mock catalogues used and the SDSS DR7 data. §5 and §6 present our fitting results and detailed tests of our fitting model and reconstruction technique on the mocks and data respectively. We present the cosmological implications of our  $D_A(z)$  and  $H(z)$  measurements in §7 and conclude in §8.

## 2 THEORY

### 2.1 Background, Basics and Definitions

There are two main effects that give rise to anisotropic galaxy clustering. The first are redshift-space distortions, which arise due to the line-of-sight velocities of galaxies such as their peculiar motions within clusters (the Finger-of-God effect) or their coherent infall towards overdense regions (Kaiser 1987). These distort our measurements of cosmological redshifts and hence the line-of-sight separation between galaxies. Such effects change the shape of the correlation function smoothly with scale (i.e. they have no features and are purely broadband in nature).

Anisotropic clustering can also arise if we assume the wrong cosmology when calculating the separations between galaxies. Since the distribution of matter is mostly isotropic at large scales, artificial anisotropies are introduced by calculating distances assuming the wrong cosmology as each cosmology predicts a unique distance scale. Specifically, we calculate line-of-sight separations using redshifts and the Hubble parameter  $H(z)$  while transverse separations are calculated using the angular separation between pairs of galaxies and the angular diameter distance  $D_A(z)$ . Both  $H(z)$  and  $D_A(z)$  are predicted given a set of cosmological parameters; however, if these do not match the true cosmology of the universe, we will measure different clustering signals along the line-of-sight and transverse directions. This implies that the BAO signal in the line-of-sight direction will be slightly offset from its location in the transverse direction. This is a manifestation of the Alcock-Paczynski technique (Alcock & Paczynski 1979), which uses the measured

anisotropy in an object thought to be isotropic to constrain the true cosmology of the universe.

In the past, limited survey volume has made it difficult to analyze the differential clustering along the line-of-sight and transverse directions. As a result, most BAO analyses have been based on the spherically-averaged (i.e. monopole) clustering statistics (e.g. Percival et al. 2010 and Padmanabhan et al. 2012), which only allow us to measure  $D_V(z)$ , the spherically-averaged distance to redshift  $z$ . This quantity is defined as

$$D_V(z) = \left[ (1+z)^2 D_A^2(z) \frac{cz}{H(z)} \right]^{1/3} \quad (1)$$

which corresponds to two powers of  $D_A(z)$  from our transverse distance measure along the two transverse directions on the sky and one power of  $H(z)$  from our line-of-sight distance measure. However, by measuring the anisotropy, we will be able to break this degeneracy between  $D_A(z)$  and  $H(z)$ , and measure these two quantities separately.

To measure the anisotropy, we must construct a clustering model that includes a parameterization of the anisotropic signal. We can then fit this model to the data and measure this parameter. Essentially one is presented with two choices. The first is to perform fits to the transverse and radial correlation functions (e.g. Okumura et al. 2008) and the second is to simultaneously fit the monopole and higher order multipoles of the clustering statistics (Padmanabhan & White 2008).

In this work, we will follow the formalism for the multipole method based on the work of Padmanabhan & White (2008). We note that the BAO can additionally be shifted in an isotropic manner if the assumed cosmology is not the true cosmology. Isotropic shifts also occur due to non-linear structure growth. We define the isotropic shift in BAO position as

$$\alpha = \frac{D_V(z)/r_s}{D_{V,f}(z)/r_{s,f}} \quad (2)$$

$$= \left[ \frac{D_A^2(z)}{D_{A,f}^2(z)} \frac{H_f(z)}{H(z)} \right]^{1/3} \frac{r_{s,f}}{r_s} \quad (3)$$

where  $D_V$  is defined as above and  $r_s$  is the sound horizon (BAO scale). The  $f$  subscripts correspond to a fiducial or reference cosmology on which we anchor our measurements: all isotropic shifts and anisotropic signals in the BAO are measured relative to this fiducial cosmology (see §3.3). This parameterization has been used extensively in past BAO studies focusing on the monopole.

We parameterize the anisotropic BAO signal as  $\epsilon$

$$1 + \epsilon = \left[ \frac{H_f(z)}{H(z)} \frac{D_{A,f}(z)}{D_A(z)} \right]^{1/3}. \quad (4)$$

These parameterizations of  $\alpha$  and  $\epsilon$  are derived from isotropic coordinate dilations and anisotropic coordinate warpings between the true and fiducial cosmology spaces (see Equations 13 & 14). Note that if there is no isotropic shift, then  $\alpha = 1$ . Similarly, the lack of anisotropy implies  $\epsilon = 0$ . Combining Equations (3) & (4), we arrive at

$$\frac{D_A(z)}{r_s} = \frac{\alpha}{1 + \epsilon} \frac{D_{A,f}(z)}{r_{s,f}} \quad (5)$$

$$H(z)r_s = \frac{1}{\alpha(1 + \epsilon)^2} H_f(z)r_{s,f}. \quad (6)$$

By measuring both the isotropic and anisotropic BAO shifts, we can separately constrain the angular diameter distance  $D_A(z)$  and the Hubble parameter  $H(z)$  at the median redshift of our galaxy sample  $z$ . If we denote the errorbars on  $\alpha$  and  $\epsilon$  as  $\sigma_\alpha$  and  $\sigma_\epsilon$ , and the covariance between them as  $\sigma_{\alpha\epsilon}$ , then the errorbars on  $D_A(z)$  and  $H(z)$  can be calculated as

$$\begin{pmatrix} \sigma_{D_A}^2 & \sigma_{D_A H} \\ \sigma_{D_A H} & \sigma_H^2 \end{pmatrix} = \begin{pmatrix} \frac{\partial D_A}{\partial \alpha} & \frac{\partial D_A}{\partial \epsilon} \\ \frac{\partial H}{\partial \alpha} & \frac{\partial H}{\partial \epsilon} \end{pmatrix} \begin{pmatrix} \sigma_\alpha^2 & \sigma_{\alpha\epsilon} \\ \sigma_{\alpha\epsilon} & \sigma_\epsilon^2 \end{pmatrix} \begin{pmatrix} \frac{\partial D_A}{\partial \alpha} & \frac{\partial D_A}{\partial \epsilon} \\ \frac{\partial H}{\partial \alpha} & \frac{\partial H}{\partial \epsilon} \end{pmatrix}^T. \quad (7)$$

This yields,

$$\frac{\sigma_{D_A}^2}{D_A^2} = \alpha^{-2} \sigma_\alpha^2 + (1 + \epsilon)^{-2} \sigma_\epsilon^2 - 2\alpha^{-1}(1 + \epsilon)^{-1} \sigma_{\alpha\epsilon} \quad (8)$$

$$\frac{\sigma_H^2}{H^2} = \alpha^{-2} \sigma_\alpha^2 + 4(1 + \epsilon)^{-2} \sigma_\epsilon^2 + 4\alpha^{-1}(1 + \epsilon)^{-1} \sigma_{\alpha\epsilon} \quad (9)$$

$$\frac{\sigma_{D_A H}}{D_A H} = -\alpha^{-2} \sigma_\alpha^2 + 2(1 + \epsilon)^{-2} \sigma_\epsilon^2 - \alpha^{-1}(1 + \epsilon)^{-1} \sigma_{\alpha\epsilon}. \quad (10)$$

We will also need a method for distinguishing between anisotropies introduced by redshift-space distortions into the broadband shape of our clustering statistic and those introduced through assuming the wrong cosmology (i.e. the Alcock-Paczynski signal). There exist simple redshift-space distortion models that can be used if we are only interested in analyzing the anisotropy in the BAO signal and not the details of the redshift-space distortions themselves. Any residual inadequate matching between these models and the actual broadband shape of the data can be mostly compensated by including a few additional marginalization terms (Seo et al. 2008; Xu et al. 2012) such as Equation (51) described in §3.3.

## 2.2 Formalism for the Correlation Function

The clustering of galaxies can be measured using the correlation function  $\xi(r)$  or the power spectrum  $P(k)$ . Since our analysis will focus on the correlation function, we will present the formalism for configuration space here and state the analogue for the power spectrum in Fourier space, which can also be found in Padmanabhan & White (2008).

We begin with a few basic coordinate definitions,

$$r^2 = r_\parallel^2 + r_\perp^2 \quad (11)$$

$$\mu^2 = \cos^2 \theta = \frac{r_\parallel^2}{r^2} \quad (12)$$

where  $r$  is the separation between two galaxies and  $\theta$  is the angle between a galaxy pair and the line-of-sight direction.  $r_\parallel$  is the separation of the galaxies in the line-of-sight direction and  $r_\perp$  is their transverse separation. In the following, unprimed coordinates will denote the fiducial cosmology space and primed coordinates will denote the true cosmology space.

The isotropic dilation ( $\alpha$ ) and anisotropic warping ( $\epsilon$ ) parameters are then defined by

$$r'_\parallel = \alpha(1 + \epsilon)^2 r_\parallel \quad (13)$$

$$r'_\perp = \alpha(1 + \epsilon)^{-1} r_\perp. \quad (14)$$

Substituting Equations (13) & (14) into the definitions

of  $r'$  and  $\mu'$  as in Equations (11) & (12), we see that

$$\begin{aligned} r' &= \alpha \sqrt{(1+\epsilon)^4 r_{\parallel}^2 + (1+\epsilon)^{-2} r_{\perp}^2} \\ &= \alpha r [1 + 2\epsilon L_2(\mu)] + \mathcal{O}(\epsilon^2) \end{aligned} \quad (15)$$

where in the last line we have substituted the second order Legendre polynomial  $L_2(\mu) = (3\mu^2 - 1)/2$ . Also,

$$\begin{aligned} \mu'^2 &= \frac{\alpha^2 (1+\epsilon)^4 r_{\parallel}^2}{\alpha^2 (1+\epsilon)^4 r_{\parallel}^2 + \alpha^2 (1+\epsilon)^{-2} r_{\perp}^2} \\ &= \mu^2 + 6\epsilon(\mu^2 - \mu^4) + \mathcal{O}(\epsilon^2). \end{aligned} \quad (16)$$

The true 2D correlation function  $\xi(\vec{r}')^2$  can be Legendre decomposed into multipole moments as

$$\xi(\vec{r}') = \sum_{\ell'=0}^{\infty} \xi_{\ell'}(r') L_{\ell'}(\mu') \quad (17)$$

where the  $L_{\ell'}(\mu')$  are Legendre polynomials of order  $\ell'$ . Again, if clustering were perfectly isotropic the  $\ell > 0$  moments would all be zero. Anisotropy introduces power into the even-order multipoles, however the odd-order multipoles are always zero due to symmetry. We can substitute Equation (15) into  $\xi_{\ell'}(r')$  and Equation (16) into  $L_{\ell'}(\mu')$  and write

$$\begin{aligned} \xi(\vec{r}') &= \sum_{\ell'=0}^{\infty} \left[ \xi_{\ell'}(\alpha r) + 2\epsilon L_2(\mu) \frac{d\xi_{\ell'}(\alpha r)}{d \log(r)} \right] \\ &\quad \cdot \left[ L_{\ell'}(\mu) + 3\epsilon \mu (1 - \mu^2) \frac{dL_{\ell'}(\mu)}{d\mu} \right], \end{aligned} \quad (18)$$

where we have made a Taylor expansion in both large brackets.

Finally, in the fiducial cosmology space, we measure the multipole moments

$$\begin{aligned} \xi_{\ell}(r) &= \frac{2\ell+1}{2} \int_{-1}^1 \xi(\vec{r}') L_{\ell}(\mu) d\mu \\ &= \xi_{\ell}(\alpha r) \\ &\quad + 3\epsilon \left[ \frac{-\ell(\ell-1)(\ell-2)}{(2\ell-3)(2\ell-1)} \xi_{\ell-2}(\alpha r) \right. \\ &\quad + \frac{\ell(\ell+1)}{(2\ell-1)(2\ell+3)} \xi_{\ell}(\alpha r) \\ &\quad \left. + \frac{(\ell+1)(\ell+2)(\ell+3)}{(2\ell+3)(2\ell+5)} \xi_{\ell+2}(\alpha r) \right] \\ &\quad + 2\epsilon \left[ \frac{3\ell(\ell-1)}{2(2\ell-3)(2\ell-1)} \frac{d\xi_{\ell-2}(\alpha r)}{d \log(r)} \right. \\ &\quad + \frac{\ell(\ell+1)}{(2\ell-1)(2\ell+3)} \frac{d\xi_{\ell}(\alpha r)}{d \log(r)} \\ &\quad \left. + \frac{3(\ell+1)(\ell+2)}{2(2\ell+3)(2\ell+5)} \frac{d\xi_{\ell+2}(\alpha r)}{d \log(r)} \right], \end{aligned} \quad (20)$$

where we have used the recursion relation for Legendre polynomials

$$(\ell+1)L_{\ell+1}(\mu) = (2\ell+1)\mu L_{\ell}(\mu) - \ell L_{\ell-1}(\mu), \quad (21)$$

the derivative relation

$$\frac{dL_{\ell}(\mu)}{d\mu} = \frac{(\ell+1)[\mu L_{\ell}(\mu) - L_{\ell+1}(\mu)]}{1-\mu^2} \quad (22)$$

and the orthogonality of Legendre polynomials

$$\int_{-1}^1 L_{\ell}(\mu) L_{\ell'}(\mu) d\mu = \frac{2}{2\ell+1} \delta_{\ell\ell'}. \quad (23)$$

Here,  $\delta_{\ell\ell'}$  is the delta function. Since we measure the correlation function using our choice of fiducial cosmology, Equation (20) will form the basis of our fitting template for extracting the isotropic dilation ( $\alpha$ ) and the anisotropic warping ( $\epsilon$ ) signal from the data.

The same relations can be derived in Fourier space from the definitions (Padmanabhan & White 2008)

$$k'_{\parallel} = \alpha^{-1} (1+\epsilon)^{-2} k_{\parallel} \quad (24)$$

$$k'_{\perp} = \alpha^{-1} (1+\epsilon) k_{\perp}. \quad (25)$$

The final equation for the measured multipole moments is identical to the configuration space case except  $\xi_{\ell}(\alpha r) \rightarrow P_{\ell}(k/\alpha)$  and the sign on each occurrence of  $\epsilon$  is flipped.

### 2.3 The Anisotropic Signal

Although anisotropic BAO information exists in all higher order multipoles, its magnitude decreases considerably. Hence, for the purposes of this study, we will only focus on the monopole ( $\ell = 0$ ) and the quadrupole ( $\ell = 2$ ). The monopole and quadrupole we expect to measure according to Equation (20) are

$$\xi_0(r) = \xi_0(\alpha r) + \frac{2}{5}\epsilon \left[ 3\xi_2(\alpha r) + \frac{d\xi_2(\alpha r)}{d \log(r)} \right] \quad (26)$$

$$\begin{aligned} \xi_2(r) &= 2\epsilon \frac{d\xi_0(\alpha r)}{d \log(r)} + \left( 1 + \frac{6}{7}\epsilon \right) \xi_2(\alpha r) + \frac{4}{7}\epsilon \frac{d\xi_2(\alpha r)}{d \log(r)} \\ &\quad + \frac{4}{7}\epsilon \left[ 5\xi_4(\alpha r) + \frac{d\xi_4(\alpha r)}{d \log(r)} \right], \end{aligned} \quad (27)$$

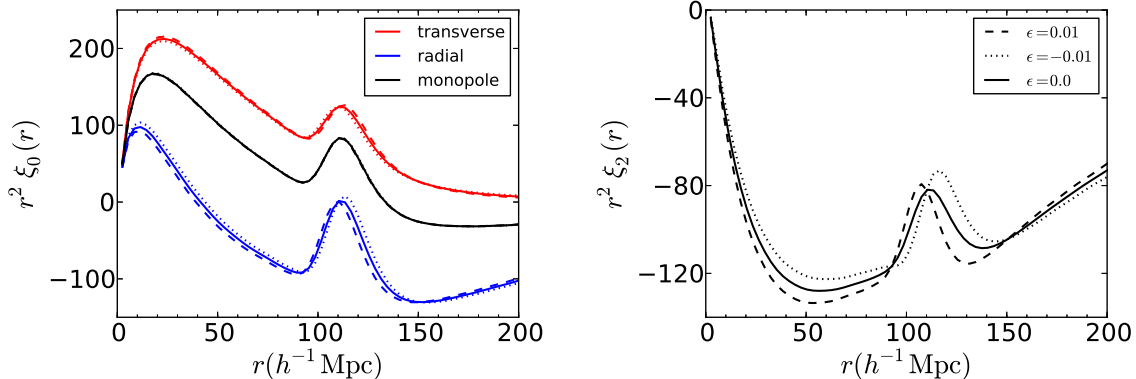
and will form the basis of our analysis. Here,  $\xi_4(r)$  is the hexadecapole ( $\ell = 4$ ).

Figure 1(a) shows variations of the expected monopole (Equation 26), the transverse and radial components of the full 2D correlation function, and the quadrupole (Equation 27) with  $\epsilon$  for a linear theory based model. For Figures 1, 2 and 3, we have assumed a cosmology with  $\Omega_b = 0.04$ ,  $\Omega_m = 0.25$ ,  $h = 0.7$ ,  $n_s = 1.0$  and  $\sigma_8 = 0.8$  (the LasDamas cosmology described in §4.1). We have included large-scale redshift-space distortions (the Kaiser effect) so that the quadrupole becomes non-zero, but not the Finger-of-God (FoG) effect. In Fourier space, this model is given by Equation (28) without the  $F(k, \mu, \Sigma_s)$  term. The transverse and radial correlation functions were calculated as  $\xi_0 + L_2(\mu)\xi_2$  for  $\mu = 0$  and 1 respectively. Note that taking the difference between these yields the quadrupole.

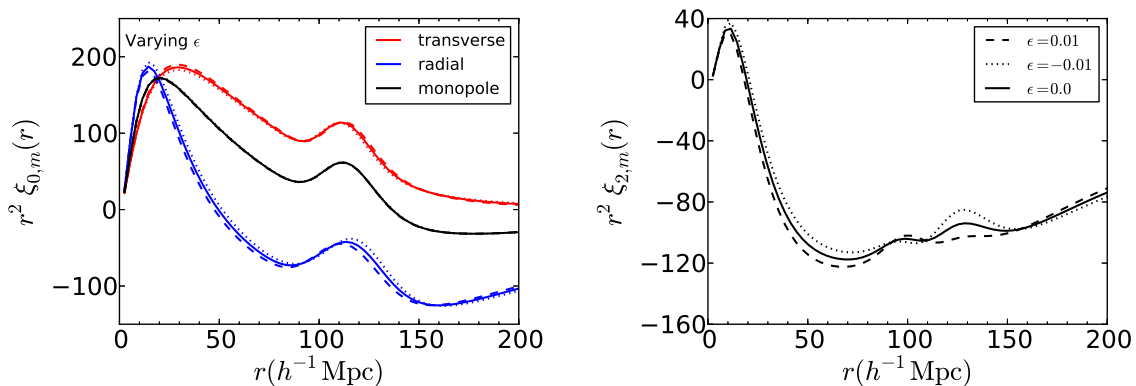
One can see that the sensitivity of the monopole to  $\epsilon$  is quite low. However  $\epsilon$  does cause significant shifts in the BAO position in the line-of-sight and transverse components of the 2D correlation function. The line-of-sight shift is larger than and opposite in direction to the transverse shift. This causes the BAO feature in the quadrupole at  $\sim 110h^{-1}$  Mpc to move with  $\epsilon$ , in addition to the shift caused by the isotropic dilation  $\alpha$ . Hence we see that the quadrupole can be used to obtain a measurement of the anisotropic BAO signal via  $\epsilon$ .

### 2.4 A Non-linear Model

In Figure 1(a) discussed in the previous section, we assumed linear theory including the Kaiser effect for  $\xi_0(r)$  and  $\xi_2(r)$ .



(a) The monopole (left) and quadrupole (right) we expect to measure in the presence of anisotropic clustering according to Equations (26) & (27) for a linear theory based model including the Kaiser effect. The Kaiser effect gives rise to the BAO bump near  $110h^{-1}\text{Mpc}$  in the quadrupole. One can see that the monopole is insensitive to  $\epsilon$ . However,  $\epsilon$  works to change the position of the line-of-sight and transverse BAO features in opposing directions with the line-of-sight having a more prominent shift. The differential nature of these shifts moves the quadrupole BAO, compounding with any isotropic shifts. Hence, we expect the quadrupole to be sensitive to an anisotropic BAO signal.



(b) Variation of monopole (left) and quadrupole (right) models including the Kaiser effect and a full non-linear treatment of FoG and anisotropic  $\Sigma_{\text{nl}}$ . The solid black line in this and the similar plots following always corresponds to the fiducial model parameters  $\Sigma_{\perp} = 6h^{-1}\text{Mpc}$ ,  $\Sigma_{\parallel} = 10h^{-1}\text{Mpc}$  and  $\Sigma_s = 4h^{-1}\text{Mpc}$  with  $\beta = 0.35$  (center of the  $\beta$  prior in our fits). The monopole is again affected very little by  $\epsilon$ . The fiducial quadrupole model picks up a crest-trough-crest structure at the BAO scale due to the differential broadening of the line-of-sight and transverse BAO signals by Kaiser, FoG and anisotropic  $\Sigma_{\text{nl}}$ . We again see that the anisotropic warping parameterized by  $\epsilon$  works to shift the location of the quadrupole BAO. In addition, it can adjust the relative amplitude of the crests.  $\epsilon$  is the only parameter that can shift the BAO in the quadrupole while leaving the monopole BAO unaffected; the isotropic shift  $\alpha$  changes the BAO position equally in both.

**Figure 1.** Variation of our models with  $\epsilon$  for a linear theory based model including the Kaiser redshift-space distortion (a) and a full non-linear model including FoG and Kaiser redshift-space distortions as well as anisotropic  $\Sigma_{\text{nl}}$  (b). In these and the following two figures, we have assumed a cosmology of  $\Omega_b = 0.04$ ,  $\Omega_m = 0.25$ ,  $h = 0.7$ ,  $n_s = 1.0$  and  $\sigma_8 = 0.8$ .  $\epsilon$  parameterizes the amount of Alcock-Paczynski anisotropy, which, if there was none, would be equal to 0. The left panel shows the monopole (black), the transverse correlation function (red) and the radial correlation function (blue), where the difference between these latter two yields a measurement of the quadrupole. Solid, dashed and dotted lines are defined as in the plot legend of the right panel which shows the quadrupole. Note that the quadrupole BAO feature is much weaker in the more realistic non-linear model.

However, in order to model actual observations with fidelity, we must also account for the FoG effect and non-linear structure growth. This section details a plausible model that includes all of these effects and will be used in our fitting procedure described in §3.3 to measure  $\alpha$  and  $\epsilon$ .

In Fourier space we can write the following template for the 2D non-linear power spectrum

$$P_t(k, \mu) = (1 + \beta\mu^2)^2 F(k, \mu, \Sigma_s) P_{\text{dw}}(k, \mu) \quad (28)$$

(Fisher et al. 1994) where

$$F(k, \mu, \Sigma_s) = \frac{1}{(1 + k^2\mu^2\Sigma_s^2)^2} \quad (29)$$

(Park et al. 1994) corresponds to a streaming model for the FoG effect and the  $(1 + \beta\mu^2)^2$  term corresponds to the Kaiser model for large-scale redshift-space distortions. Here  $\Sigma_s$  is the streaming scale and is typically  $\sim 3 - 4h^{-1}\text{Mpc}$ .

The de-wiggled power spectrum  $P_{\text{dw}}(k, \mu)$  is defined as

$$P_{\text{dw}}(k, \mu) = [P_{\text{lin}}(k) - P_{\text{nw}}(k)] \cdot \exp\left[-\frac{k^2\mu^2\Sigma_{\parallel}^2 + k^2(1-\mu^2)\Sigma_{\perp}^2}{2}\right] + P_{\text{nw}}(k) \quad (30)$$

(Eisenstein, Seo & White 2007) where  $P_{\text{lin}}(k)$  is the linear theory power spectrum and  $P_{\text{nw}}(k)$  is a power spectrum without an acoustic signature (Eisenstein & Hu 1998).  $\Sigma_{\parallel}$  and  $\Sigma_{\perp}$  are the line-of-sight and transverse components of  $\Sigma_{\text{nl}}$ , i.e.  $\Sigma_{\text{nl}}^2 = (\Sigma_{\parallel}^2 + \Sigma_{\perp}^2)/2$ , where  $\Sigma_{\text{nl}}$  is the standard Gaussian damping of the BAO used to model the degradation of the signal due to non-linear structure growth (Eisenstein, Seo & White 2007). Here, the damping is anisotropic due to the Kaiser effect.

The multipoles of this template are then

$$P_{\ell,t}(k) = \frac{2\ell+1}{2} \int_{-1}^1 P_t(k, \mu) L_{\ell}(\mu) d\mu, \quad (31)$$

which can be transformed to configuration space using

$$\xi_{\ell,t}(r) = i^{\ell} \int \frac{k^3 d \log(k)}{2\pi^2} P_{\ell,t}(k) j_{\ell}(kr). \quad (32)$$

Figure 1(b) shows the variation of our non-linear monopole and quadrupole models with  $\epsilon$  while Figure 2 shows the variations with other parameters. The variation with  $\alpha$  is not shown as its role is well understood:  $\alpha$  works to shift the BAO feature around equally in both the monopole and quadrupole. Figure 2(a) shows the variations with  $\Sigma_{\perp}$  and  $\Sigma_{\parallel}$ . Figure 2(b) shows the variations with  $\Sigma_s$  and Figure 2(c) shows the variations with  $\beta$ . In these plots, the solid black line always corresponds to the fiducial model parameters  $\Sigma_{\perp} = 6h^{-1}\text{Mpc}$ ,  $\Sigma_{\parallel} = 10h^{-1}\text{Mpc}$  and  $\Sigma_s = 4h^{-1}\text{Mpc}$ .  $\beta$  is set to the center of the prior, 0.35, unless indicated otherwise. These fiducial parameters will be discussed in more detail in §3.3.

We see that the monopole model is only weakly affected by varying these parameters.  $\Sigma_{\text{nl}}$  has an immediately obvious effect on the BAO peak since it is designed to damp the BAO to model non-linear evolution. The change in the peak is only significant with a large change in  $\Sigma_{\text{nl}}$ . The  $\Sigma_{\perp} = \Sigma_{\parallel} = 8h^{-1}\text{Mpc}$  case and the fiducial case have very similar  $\Sigma_{\text{nl}}$  values. Hence, we see little difference between the monopole models in these two cases. However, the  $\Sigma_{\perp} = 4h^{-1}\text{Mpc}$ ,  $\Sigma_{\parallel} = 7h^{-1}\text{Mpc}$  case corresponds to  $\Sigma_{\text{nl}} \sim 6h^{-1}\text{Mpc}$  which affords a weaker smearing of the peak. Large  $\Sigma_s$  values can also weakly damp the monopole BAO, causing slight modifications to its shape.  $\beta$  appears to have little effect on the monopole and  $\epsilon$  has no effect. The only parameter that can shift the monopole BAO position is  $\alpha$ , which also shifts the quadrupole BAO equally.

Looking at the quadrupole model in the fiducial case, we see that the BAO (at  $r \sim 110h^{-1}\text{Mpc}$ ) looks different from the case presented in Figure 1(a). There we saw a single bump at the acoustic scale due to the Kaiser anisotropy  $(1 + \beta\mu^2)^2$ . Including FoG and anisotropic  $\Sigma_{\text{nl}}$  introduces more structure at the BAO scale. We see that in the fiducial model, a dip has appeared at the center of the linear-theory peak, creating a crest-trough-crest structure. This is the result of anisotropic  $\Sigma_{\text{nl}}$ ,  $\Sigma_s$  and  $\beta$  differentially broadening the BAO peak in the radial and line-of-sight directions. We

see that the radial BAO is wider than the transverse BAO, but the radial BAO peak has more contrast. Subtracting the two therefore yields the observed crest-trough-crest shape of the quadrupole near the BAO.

Figure 2(a) shows that changing  $\Sigma_{\perp}$  and  $\Sigma_{\parallel}$  gives rise to crests and troughs near the BAO scale in the quadrupole. Taking  $\Sigma_{\text{nl}}$  to be isotropic and non-zero completely removes the trough, leaving a single peak that is broader than the linear-theory case. Changing the values of  $\Sigma_{\perp}$  and  $\Sigma_{\parallel}$  (but keeping their ratios roughly the same) alters the structure of the peaks and changes the crest-trough contrast.

Changing  $\Sigma_s$  has the most prominent effects at small scales as expected, since the FoG is strongest there. It also causes a noticeable change in the quadrupole BAO signal which is partially degenerate with the effects of anisotropic  $\Sigma_{\text{nl}}$ , i.e. it can also adjust the crest-trough contrast and can eliminate the trough entirely ( $\Sigma_s = 0h^{-1}\text{Mpc}$ ). Leverage on this parameter mostly comes from small scales, where  $\Sigma_s$  has a significant effect on the quadrupole shape.

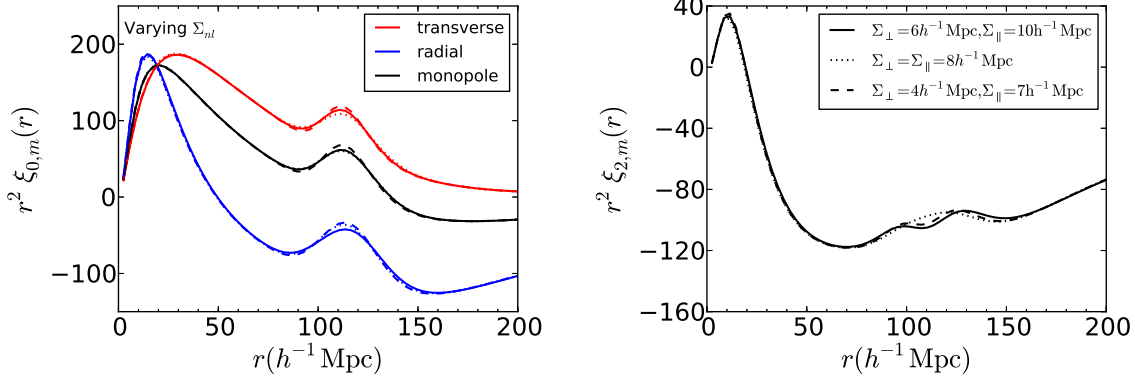
Changing  $\beta$  shifts the overall magnitude of the quadrupole at large scales. Hence, we see that varying  $\Sigma_{\perp}$ ,  $\Sigma_{\parallel}$ ,  $\Sigma_s$  and  $\beta$  only affects the shape of the quadrupole, not the BAO position.

Only  $\epsilon$  and  $\alpha$  can shift the location of the BAO. While  $\alpha$  shifts the BAO position equally along all directions, Figure 1(b) shows that  $\epsilon$  shifts the radial BAO position more than and in the opposite direction to the transverse BAO position. Therefore changing  $\epsilon$  will cause the quadrupole BAO position to change in addition to the shift induced by  $\alpha$ . We see from 1(b) that  $\epsilon$  can also adjust the BAO shape so it is not completely non-degenerate with the other parameters. We emphasize that  $\Sigma_{\perp}$ ,  $\Sigma_{\parallel}$ ,  $\Sigma_s$  and  $\beta$  cannot shift the quadrupole BAO, they merely work to change the BAO shape.  $\epsilon$  is the only parameter that can change the quadrupole BAO position without changing the monopole BAO position, so its effects should be detectable.

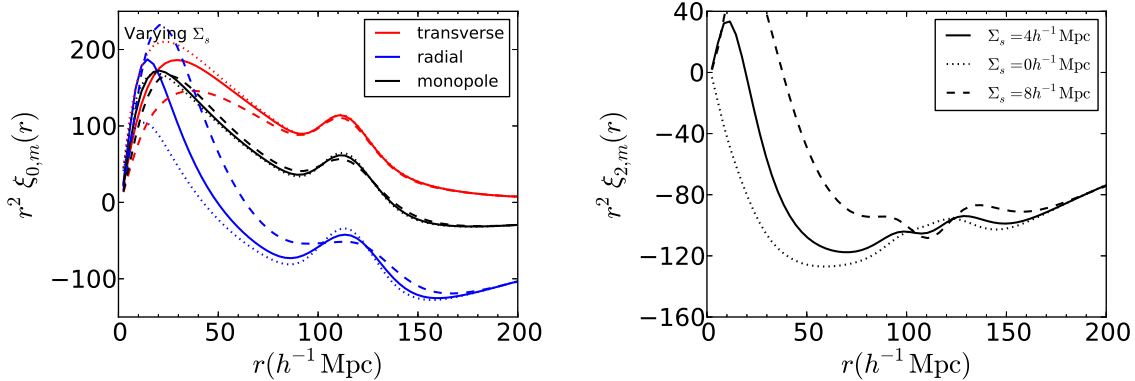
The above observations of the model quadrupole behaviour can be re-cast into Figure 3. The panels of this figure show the derivatives of the quadrupole model with respect to each parameter ( $\Sigma_{\perp}$  - top left,  $\Sigma_{\parallel}$  - top right,  $\Sigma_s$  - middle left,  $\beta$  - middle right,  $\alpha$  - bottom left and  $\epsilon$  - bottom right). The dashed line marks the acoustic scale. The plotted derivatives show the variation of the model with these parameters and are especially interesting near the acoustic scale.

One can see that the behaviour of the  $\Sigma_{\perp}$  derivative near the BAO scale is exactly opposite to the  $\Sigma_{\parallel}$  case. In the former we see a down-up-down structure and in the latter we see an up-down-up structure. The  $\Sigma_s$  derivative shows similar behaviour to the  $\Sigma_{\parallel}$  derivative near the acoustic scale. However, its small-scale behaviour is much different. The  $\beta$  derivative shows only a single peak near the acoustic scale. Note that all of these derivatives are symmetric about the acoustic scale.

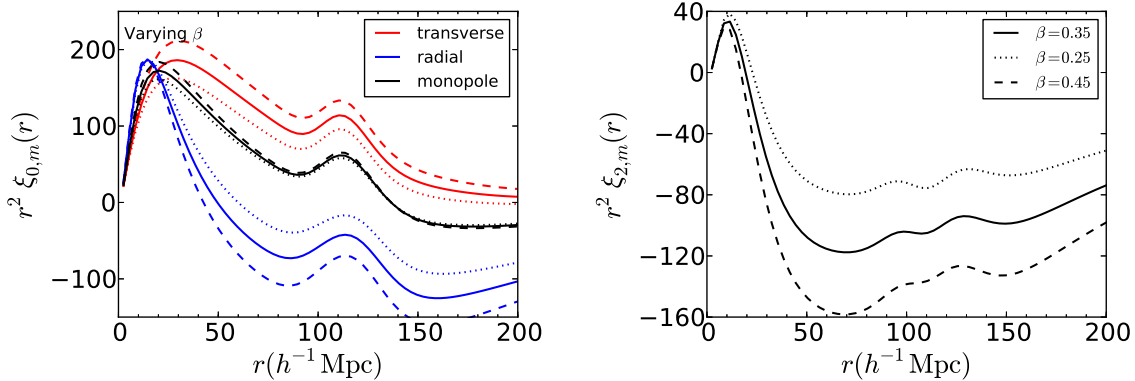
The  $\alpha$  and  $\epsilon$  derivatives are different from the others in that they are both anti-symmetric about the acoustic scale. This reflects their ability to shift the BAO feature. The difference between  $\alpha$  and  $\epsilon$  lies mainly in the monopole where  $\alpha$  can significantly shift the BAO but  $\epsilon$  cannot;  $\epsilon$  only shifts the BAO in the quadrupole. Near the acoustic scale, the quadrupole  $\alpha$  derivative shows a large amount of structure while the  $\epsilon$  derivative shows a simple up-down structure.



(a) Variation of the monopole (left) and quadrupole (right) models with  $\Sigma_{\perp}$  and  $\Sigma_{\parallel}$ . The BAO peak in the monopole can be affected by  $\Sigma_{\text{nl}}$  as expected since this parameter is used to model the smearing of the BAO due to non-linear structure growth. In these plots we have demonstrated the effects of going to an isotropic  $\Sigma_{\text{nl}}$  of roughly the same magnitude as the fiducial case (dotted line) and a smaller  $\Sigma_{\text{nl}}$  (dashed line). We see that going to an isotropic  $\Sigma_{\text{nl}}$  has little effect on the monopole, however, it completely eliminates the trough feature at the BAO scale in the quadrupole. Going to a smaller  $\Sigma_{\text{nl}}$  makes the peak appear sharper in the monopole as expected. In the quadrupole, it alters the structure of the peaks and reduces the crest-trough contrast.



(b) Variation of the monopole (left) and quadrupole (right) models with  $\Sigma_s$ . The BAO feature in the monopole can be slightly broadened by a large  $\Sigma_s$ . In the quadrupole, the effects of  $\Sigma_s$  are partially degenerate with  $\Sigma_{\text{nl}}$  in that it can alter the crest-trough contrast and can also completely eliminate the trough ( $\Sigma_s = 0h^{-1}\text{Mpc}$ ). However, the effects of  $\Sigma_s$  are much stronger at small scales due to its large influence on the radial and transverse correlation functions, giving us leverage on this parameter. These variations are not surprising since the FoG effect is most pronounced at smaller scales.



(c) Variation of the monopole (left) and quadrupole (right) models with  $\beta$ . Again we see that the monopole is not significantly affected by  $\beta$ . The line-of-sight and transverse correlation functions experience large changes in amplitude with  $\beta$ , leading to amplitude differences in the quadrupole at large scales.

**Figure 2.** Variation of the non-linear monopole and quadrupole models with different model parameters:  $\Sigma_{\text{nl}}$  (a),  $\Sigma_s$  (b) and  $\beta$  (c). Comparing the behaviour of these parameters to  $\epsilon$  (Figure 1(b)) indicates that the various model parameters have mostly different effects on the quadrupole. While all of these parameters can affect the shape of the quadrupole, only  $\epsilon$  can change the quadrupole BAO position separately from the monopole BAO ( $\alpha$  changes both in lock-step). Hence we expect that the effects of  $\epsilon$  should be detectable.

The crests and troughs of both of these will be partially degenerate with the other parameters despite their opposite symmetries near the acoustic scale. However, if we place well-informed priors on the other parameters, we limit the model from exploring these degeneracies thereby obtaining reasonably robust measurements of  $\epsilon$ .

A similar conclusion can be reached by noting that the first three cases look like the derivative of a Gaussian with respect to its width. The  $\beta$  case looks like the derivative of a Gaussian with respect to its height and the  $\epsilon$  case looks like the derivative of a Gaussian with respect to its center. All of these behaviours are different.

## 2.5 Covariance Matrix Formalism

The simplest analytic form for the  $\xi(r)$  covariance matrix assumes that primordial overdensities are drawn from a Gaussian random field in which all Fourier modes grow independently. In this limit, the covariance between two multipole moments  $\ell$  and  $\ell'$  is

$$C_{ij}(\xi_\ell(r_i), \xi_{\ell'}(r_j)) = \frac{2(2\ell+1)(2\ell'+1)}{V} \cdot \int \frac{k^3 d \log(k)}{2\pi^2} j_\ell(kr_i) j_{\ell'}(kr_j) P_{\ell\ell'}^2(k) \quad (33)$$

where  $V$  is the survey volume, the  $j_\ell(kr)$  are the spherical Bessel functions of order  $\ell$  and  $P_{\ell\ell'}^2(k)$  is defined as

$$P_{\ell\ell'}^2(k) = \frac{1}{2} \int_{-1}^1 \left[ P(k, \mu) + \frac{1}{\bar{n}} \right]^2 L_\ell(\mu) L_{\ell'}(\mu) d\mu. \quad (34)$$

Here,  $P(k, \mu)$  is the 2D power spectrum and  $\bar{n}$  is the mean number density of galaxies. The  $1/\bar{n}$  term corresponds to Poisson shot-noise. However, it is well-known that non-linear structure growth introduces coupling between the various modes (Meiksin, White & Peacock 1999; Seo & Eisenstein 2005; Jeong & Komatsu 2006; Eisenstein, Seo & White 2007; Huff et al. 2007; Guzik, Bernstein & Smith 2007; Ma 2007; Angulo et al. 2008; Crocce & Scoccimarro 2008; Sanchez, Baugh & Angulo 2008; Seo et al. 2008; Smith, Scoccimarro, & Sheth 2008; Padmanabhan & White 2009; Takahashi et al. 2009). These effects can be largely included by using non-linear models for the 2D power spectrum and shot-noise terms (e.g. as shown in Xu et al. 2012). In the above, we have also ignored the redshift dependence of  $\bar{n}$  above, however, we will describe a method that allows its inclusion in §3.3.

In practice, the correlation functions we measure are binned and hence, we must also account for this binning in the Gaussian covariance matrix. If we calculate the correlation function in bins with lower bounds  $r_1$  and upper bounds  $r_2$ , the binned covariance matrix is

$$C_{ij}(\xi_\ell(r_i), \xi_{\ell'}(r_j)) = \frac{2(2\ell+1)(2\ell'+1)}{V} \frac{3}{r_{i2}^3 - r_{i1}^3} \frac{3}{r_{j2}^3 - r_{j1}^3} \cdot \int_{r_{i1}}^{r_{i2}} r^2 dr \frac{d\Omega}{4\pi} \int_{r_{j1}}^{r_{j2}} r'^2 dr' \frac{d\Omega'}{4\pi} \cdot \int \frac{k^3 d \log(k)}{2\pi^2} j_\ell(kr) j_{\ell'}(kr') P_{\ell\ell'}^2(k). \quad (35)$$

In the case of the monopole and quadrupole relevant to this study, the above expression can be split into the  $\ell = \ell' = 0$  case, the  $\ell = 0$  and  $\ell' = 2$  (or vice versa) case and the  $\ell = \ell' = 2$ . The first case was shown to have the form (Xu et al. 2012)

$$C_{ij}(\xi_0(r_i), \xi_0(r_j)) = \frac{2}{V} \int \frac{k^3 d \log(k)}{2\pi^2} \mathcal{J}_0(kr_i) \mathcal{J}_0(kr_j) P_{00}^2(k) \quad (36)$$

where

$$\mathcal{J}_0(kr) = \frac{3}{r_2^3 - r_1^3} \left[ \frac{r^2 j_1(kr)}{k} \right]_{r_1}^{r_2} \quad (37)$$

and

$$j_1(kr) = \frac{\sin(kr)}{(kr)^2} - \frac{\cos(kr)}{kr}. \quad (38)$$

Here,  $[f(x)]_b^a$  is standard notation for  $f(a) - f(b)$  for any function  $f$ . The second case has the form

$$C_{ij}(\xi_0(r_i), \xi_2(r_j)) = \frac{10}{V} \int \frac{k^3 d \log(k)}{2\pi^2} \mathcal{J}_0(kr_i) \mathcal{J}_2(kr_j) P_{02}^2(k) \quad (39)$$

where

$$\mathcal{J}_2(kr) = \frac{3}{r_2^3 - r_1^3} \left[ \frac{3\text{si}(kr)}{k^3} - \frac{1}{k} \left( \frac{3r}{k} j_0(kr) + r^2 j_1(kr) \right) \right]_{r_1}^{r_2}, \quad (40)$$

$$\text{si}(x) = \int_0^x \frac{\sin(x')}{x'} dx' \quad (41)$$

and

$$j_0(kr) = \frac{\sin(kr)}{kr}. \quad (42)$$

Note that due to symmetry, we have  $C_{ij}(\xi_0(r_i), \xi_2(r_j)) = C_{ij}(\xi_2(r_i), \xi_0(r_j))$ . Finally, the last case has the form

$$C_{ij}(\xi_2(r_i), \xi_2(r_j)) = \frac{50}{V} \int \frac{k^3 d \log(k)}{2\pi^2} \mathcal{J}_2(kr_i) \mathcal{J}_2(kr_j) P_{22}^2(k). \quad (43)$$

Collectively, we can then write

$$C_{ij}(\xi_\ell(r_i), \xi_{\ell'}(r_j)) = \frac{2(2\ell+1)(2\ell'+1)}{V} \cdot \int \frac{k^3 d \log(k)}{2\pi^2} \mathcal{J}_\ell(kr_i) \mathcal{J}_{\ell'}(kr_j) P_{\ell\ell'}^2(k). \quad (44)$$

These forms for the binned Gaussian covariance matrix form the basis for deriving a covariance matrix for our data. We extend the method for approximating the mock covariances using a modified form of the binned Gaussian covariance matrix as described in Xu et al. (2012). This will be outlined in §3.3.

## 3 ANALYSIS

### 3.1 Reconstruction

Non-linear structure growth degrades and shifts the acoustic peak. Reconstruction was initially proposed to partially remove these effects (Eisenstein et al. 2007). In the linear theory description of structure growth, overdensities are small and hence remain largely in place as they accrete more



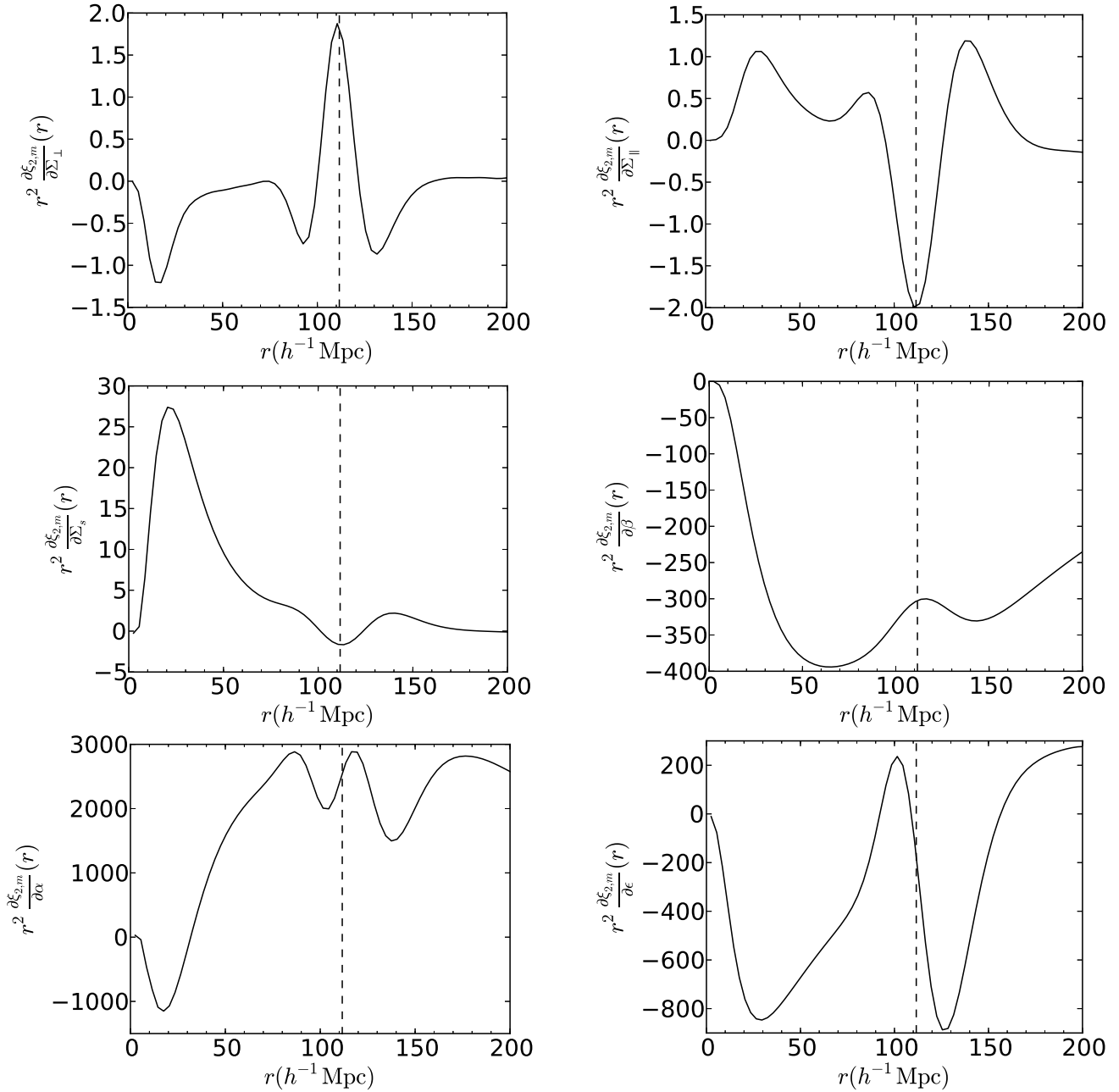


**Figure 3.** Derivatives of the model quadrupole with respect to  $\Sigma_{\perp}$  (top left),  $\Sigma_{\parallel}$  (top right),  $\Sigma_s$  (middle left),  $\beta$  (middle right),  $\alpha$  (bottom left) and  $\epsilon$  (bottom right). The plotted derivatives illustrate how the model changes with these various parameters and is especially interesting near the BAO scale marked by the dashed line. Note that near the acoustic scale, the  $\Sigma_{\perp}$ ,  $\Sigma_{\parallel}$  and  $\Sigma_s$  cases look like derivatives of a Gaussian with respect to its width. The  $\beta$  case looks like the derivative of a Gaussian with respect to its height. The  $\epsilon$  case looks like the derivative of a Gaussian with respect to its center. These behaviours are all different. We see that the  $\Sigma_{\perp}$  and  $\Sigma_{\parallel}$  derivatives are similar in nature at the acoustic scale but opposite in sign. The  $\Sigma_{\parallel}$  and  $\Sigma_s$  derivatives, however, are of the same sign and show the same up-down-up structure near the BAO scale, but differ at small scales. The  $\beta$  derivative only shows a single peak near the acoustic scale. We also see that the  $\Sigma_{\perp}$ ,  $\Sigma_{\parallel}$ ,  $\Sigma_s$  and  $\beta$  derivatives are symmetric about the acoustic scale while the  $\alpha$  and  $\epsilon$  derivatives are anti-symmetric. The  $\alpha$  derivative has the most structure near the acoustic scale. The  $\epsilon$  derivative shows a simple up-down structure. Despite their opposite symmetries near the acoustic scale, the various crests and troughs of the  $\alpha$  and  $\epsilon$  derivatives will be partially degenerate with the other parameters. However, given reasonable priors on the other parameters, the model will not be allowed to explore these degeneracies and we will recover robust measurements of  $\epsilon$ .

matter and grow. However, at low redshifts, this description becomes increasingly less suitable as some overdensities grow to masses large enough that they begin exerting significant gravitational pulls on each other. This gives rise to pairwise relative velocities between particles separated by  $\sim 100h^{-1}\text{Mpc}$ . These coherent flows that form large-scale structure are the dominant source of smearing of the BAO signal. The peculiar motions of particles within a gravitationally bound structure are subdominant. Reconstruction attempts to undo these coherent motions in the matter density field and arrive back at something that more closely resembles linear theory. This translates into a sharpening up of the acoustic peak in the correlation function which allows us to gain a better centroiding of its location and hence a more precise measure of the acoustic scale. It also removes some of the shifting of the BAO due to non-linear structure growth, which has been shown to be a  $\sim 0.5\%$  effect at  $z = 0$  (Seo et al. 2010; Mehta et al. 2011).

Our reconstruction algorithm is described in detail in Padmanabhan et al. (2012). A more pedagogical discussion of reconstruction can also be found there. This method is extended from the original reconstruction algorithm proposed in Eisenstein et al. (2007) and its theoretical basis is established in Padmanabhan, White & Cohn (2009) and Noh, White & Padmanabhan (2009). A basic outline is given below.

The ultimate goal of reconstruction is to infer the matter displacement field that arises due to non-linear structure growth from the observed galaxy density field. Then, we can shift the galaxies back along their inferred displacement vectors to place them where they would have been in linear theory. This is simple if we consider only the first order displacements  $\Psi$ . In this case

$$\nabla \cdot \Psi + \beta \nabla \cdot (\Psi_s \hat{\mathbf{s}}) = -\frac{\delta_{\text{gal}}}{b} \quad (45)$$

where  $\Psi_s = \Psi \cdot \hat{\mathbf{s}}$  is the displacement in the line-of-sight direction (Nusser & Davis 1994),  $\delta_{\text{gal}}$  is the galaxy density field,  $b$  is the large-scale galaxy bias (which is roughly constant) and hence  $\delta_{\text{gal}}/b$  is an approximation of the matter density field. The second term in this equation arises due to large-scale redshift-space distortions caused by the coherent infall of galaxies towards overdense regions (Kaiser 1987). This implies that as an additional bonus, reconstruction can also correct for linear redshift-space distortions. The  $\beta$  parameter governs the amount of anisotropy introduced by the Kaiser effect. It is defined as  $\beta = f/b$  where  $f = d \log D(a)/d \log(a) \sim \Omega_m(a)^{0.55}$  is the linear growth rate,  $D(a)$  is the linear growth function and  $a$  is the scale factor (Caroll, Press & Turner 1992; Linder 2005). If we assume that  $\Psi$  is irrotational (i.e. curl-free), we can write  $\Psi = \nabla \phi$ . After selecting appropriate values of  $b$  and  $\beta$ , we can solve for the scalar field  $\phi$  and then the displacement field  $\Psi$  using a finite difference approach.

Areas that do not fall within the survey or are masked out by the survey need to be accounted for as the gravitational potential (and hence the displacement field) is sensitive to these regions. We embed the survey into a larger Gaussian realization (Hoffman & Ribak 1991; Zaroubi et al. 1995) constrained to match the density field where observed. The exact implementation is described in detail in Padmanabhan et al. (2012), and we refer the reader to the

description there for more details. When doing this embedding, one has a choice to either set unconstrained Fourier modes to zero (Wiener filtering) or sample them from an assumed power spectrum. We explicitly show that our distance constraints do not depend on this choice in §5.

### 3.2 Computation

The computation of our correlation functions is tied to our reconstruction algorithm. We bin our correlation functions in  $3h^{-1}\text{Mpc}$  bins starting at  $2.5h^{-1}\text{Mpc}$  and going up to  $197.5h^{-1}\text{Mpc}$ . A list of the steps involved is given below.

- I) Obtain a set of randomly distributed points that have the same angular and radial selection function as the survey.
- II) Compute the unreconstructed correlation function from the data using the Landy-Szalay estimator (Landy & Szalay 1993),

$$\xi(r, \mu) = \frac{DD(r, \mu) - 2DR(r, \mu) + RR(r, \mu)}{RR(r, \mu)} \quad (46)$$

where  $DD$ ,  $DR$  and  $RR$  are the number of galaxy-galaxy, galaxy-random and random-random pairs that are separated by  $r$  and  $\mu$ . We apply FKP weighting (Feldman, Kaiser & Peacock 1994) for each object as

$$w_i = \frac{1}{1 + \bar{n}(z_i)P(k_0)} \quad (47)$$

where  $\bar{n}(z_i)$  is the number density at the redshift of the object  $z_i$  and  $P(k_0) = 40000h^{-3} \text{Mpc}^3$  is the approximate value of the power spectrum at the BAO scale.

- III) Estimate the galaxy bias  $b$  and the anisotropy parameter  $\beta$  from the unreconstructed correlation function. We use fiducial values of  $b = 2.2$  and  $\beta = 0.3$ .

IV) Embed the survey in a larger volume and smooth the density field using a Gaussian (again, we use a smoothing length of  $15h^{-1}\text{Mpc}$ ). Generate a constrained Gaussian realization matching the observed density to fill in the masked and unobserved regions.

- V) Estimate the displacement field  $\Psi$  using Equation (45) and shift the galaxies by  $-\Psi - f(\Psi_s \hat{\mathbf{s}})$  to partially undo the effects of non-linear structure growth and large-scale redshift-space distortions. This is the essence of reconstruction.

VI) Obtain another set of randomly generated particles with the same radial and angular selection function as the survey. Shift these by  $-\Psi$  and denote as  $S$ .

- VII) Compute the reconstructed correlation function using the Landy-Szalay estimator

$$\xi(r, \mu) = \frac{DD(r, \mu) - 2DS(r, \mu) + SS(r, \mu)}{RR(r, \mu)}. \quad (48)$$

### 3.3 Fitting

We construct models of the monopole and quadrupole in a fiducial cosmology to measure the position of the BAO in the data relative to the model (parameterized by  $\alpha$ ) and the degree to which it is anisotropic in the data (parameterized by  $\epsilon$ ). We base our fitting templates for the monopole and quadrupole on Equations (26) & (27). That is, we define

fitting models of the form

$$\xi_{0,m}(r) = B_0^2 \xi_{0,t}(\alpha r) + \frac{2}{5} \epsilon \left[ 3\xi_{2,t}(\alpha r) + \frac{d\xi_{2,t}(\alpha r)}{d \log(r)} \right] + A_0(r) \quad (49)$$

$$\begin{aligned} \xi_{2,m}(r) &= 2B_0^2 \epsilon \frac{d\xi_{0,t}(\alpha r)}{d \log(r)} + \left( 1 + \frac{6}{7} \epsilon \right) \xi_{2,t}(\alpha r) + \frac{4}{7} \epsilon \frac{d\xi_{2,t}(\alpha r)}{d \log(r)} \\ &+ \frac{4}{7} \epsilon \left[ 5\xi_{4,t}(\alpha r) + \frac{d\xi_{4,t}(\alpha r)}{d \log(r)} \right] + A_2(r) \end{aligned} \quad (50)$$

where

$$A_\ell(r) = \frac{a_{\ell,1}}{r^2} + \frac{a_{\ell,2}}{r} + a_{\ell,3}. \quad (51)$$

The  $A_\ell(r)$  are composed of linear nuisance terms used to marginalize out broadband effects such as scale-dependent bias and redshift-space distortions as in Xu et al. (2012). The  $B_0^2$  term adjusts the amplitude of the monopole template  $\xi_{0,t}$ . We infer the galaxy bias  $b$  from the multiplicative offset,  $b^2$ , between this template and the measured correlation function at  $r = 50h^{-1}\text{Mpc}$ . We then use this offset to normalize the full models,  $\xi_{0,m}$  and  $\xi_{2,m}$  in Equations (49) & (50), to the data. This ensures that  $B_0^2 \sim 1$  as it is primarily the monopole fit that sets this term and  $\epsilon$  is very small. In practice we perform our fits in the non-linear parameter  $\log(B_0^2)$  to prevent  $B_0^2$  from going negative which would be unphysical. We adopt a Gaussian prior on  $\log(B_0^2)$  with standard deviation 0.4 and centered at 0 to prevent  $B_0^2$  from wandering too far from 1 as described in Xu et al. (2012).

In addition, we apply a 10% Gaussian prior on  $1 + \epsilon$  to limit noise from dragging  $\epsilon$  to unrealistically large values. In fitting the mocks without the prior, only 2 have measured  $\epsilon$  values  $> 0.1$ , so this prior does not have a significant impact. To verify that this prior is not cosmologically important, we use the CMB+allBAO  $ow_0wa$ CDM Markov Chain Monte Carlo results from Mehta et al. (2012) to estimate the allowed distribution of  $\epsilon$ . The distribution is nearly Gaussian with a standard deviation of  $\sim 0.026$  which is much less than our 0.1 prior.

The monopole and quadrupole correlation function templates ( $\xi_{0,t}(r)$  and  $\xi_{2,t}(r)$ ) are derived from the 2D power spectrum  $P_t(k, \mu)$  template (Equation 28) as described in §2.4. We set  $\Sigma_s = 4h^{-1}\text{Mpc}$ . We let  $\beta$  vary in our fits as it affords us leverage on the amplitude of the quadrupole with which it is partially degenerate. We put a prior on  $\beta$  centered at  $f/b \sim \Omega_m(z)^{0.55}/b = 0.35$  before reconstruction and 0 after reconstruction with 0.2 standard deviation in both cases. The choice of  $\beta = 0$  as the center of the prior after reconstruction is because we expect the Kaiser effect to be mostly removed. We fix  $\Sigma_\perp = 6h^{-1}\text{Mpc}$  and  $\Sigma_\parallel = 10h^{-1}\text{Mpc}$  in our pre-reconstruction fits and  $\Sigma_\perp = \Sigma_\parallel = 3h^{-1}\text{Mpc}$  in our post-reconstruction fits. These values are approximated from the fit results to the average correlation function of the mocks where we set  $\Sigma_\parallel = (1+f)\Sigma_\perp$  in the pre-reconstruction case due to the Kaiser effect and  $\Sigma_\parallel = \Sigma_\perp$  in the post-reconstruction case due to the expected removal of Kaiser squashing by reconstruction.

We simultaneously fit the monopole and the quadrupole for 4 non-linear parameters  $\log(B_0^2)$ ,  $\beta$ ,  $\alpha$  and  $\epsilon$ , in addition to the linear nuisance parameters in  $A_\ell(r)$ . The non-linear parameters are handled using a simplex algorithm and the linear parameters are obtained using a least-squares method nested within this simplex. That is, for each set of non-

linear parameters, the least-squares algorithm returns the corresponding best-fit linear parameters. The simplex steps through the non-linear parameter space until the best-fit values are obtained. To determine the best-fit values, we minimize the  $\chi^2$  goodness-of-fit indicator given by

$$\chi^2 = (\vec{m} - \vec{d})^T C^{-1} (\vec{m} - \vec{d}) \quad (52)$$

where  $\vec{m}$  is a column vector of the model at each step in the simplex and  $\vec{d}$  is the data. Both of these must contain both the monopole and quadrupole values in sequence.  $C$  is the covariance matrix described below. We use a fiducial fitting range of  $50 < r < 200h^{-1}\text{Mpc}$  which corresponds to fitting 50 points in both the monopole and the quadrupole. This gives  $2 \times 50 - \#$  of fit parameters =  $100 - 10 = 90$  degrees-of-freedom (dof) in the fit. Using this technique we obtain best-fit values of our parameters of interest, the isotropic dilation  $\alpha$  and the anisotropic warping  $\epsilon$  of the BAO signal.

In addition, we can calculate the probability distribution  $p(\alpha, \epsilon)$  by fitting for the other parameters at various grid values of these two parameters and measuring the best-fit  $\chi^2$ . This is feasible because  $p(\vec{x}) \propto \exp(-\chi^2/2)$ . The constant of proportionality corresponds to the normalization that makes the integral  $\int p(\vec{x}) d\vec{x} = 1$ . Then we can calculate  $p(\alpha)$  and  $p(\epsilon)$  as

$$p(\alpha) = \int p(\alpha, \epsilon) d\epsilon \quad (53)$$

$$p(\epsilon) = \int p(\alpha, \epsilon) d\alpha. \quad (54)$$

We can take the widths of these distributions ( $\sigma_\alpha$  and  $\sigma_\epsilon$ ) as measurements of the errors on  $\alpha$  and  $\epsilon$  if  $\alpha$  and  $\epsilon$  have Gaussian posteriors. In §5 we demonstrate using fit results to our mock catalogues that  $\alpha$  and  $\epsilon$  are consistent with having been drawn from Gaussian distributions. The covariance between  $\alpha$  and  $\epsilon$  ( $C_{\alpha\epsilon}$ ) can also be calculated and converted into a correlation coefficient  $\rho_{\alpha\epsilon}$ . These are defined

$$\sigma_x^2 = \int p(x)(x - \langle x \rangle)^2 dx \quad (55)$$

$$C_{\alpha\epsilon} = \int \int p(\alpha, \epsilon)(\alpha - \langle \alpha \rangle)(\epsilon - \langle \epsilon \rangle) d\alpha d\epsilon \quad (56)$$

$$\rho_{\alpha\epsilon} = \frac{C_{\alpha\epsilon}}{\sigma_\alpha \sigma_\epsilon} \quad (57)$$

where  $\langle x \rangle$  is the mean of the distribution  $p(x)$ . For our grids we pick the ranges  $0.7 < \alpha < 1.3$  and  $-0.3 < \epsilon < 0.3$  at spacings of 0.0025 and 0.005 respectively. We also apply an additional Gaussian prior on  $\log(\alpha)$  with a width of 0.15 to suppress any unphysical downturns in the  $\chi^2$  distribution at small  $\alpha$ . These  $\alpha$  correspond to the acoustic peak in the model being pushed out to larger scales where the fitter has an easier time hiding the peak in the large errorbars. This procedure was scrutinized in detail in Xu et al. (2012). Note that our grids are only used to compute  $p(\alpha)$  and  $p(\epsilon)$ . We do not use them to infer the best-fit values of these parameters, which are obtained through the non-linear simplex optimization described above.

We obtain a smooth estimate of the covariance matrix using the method described in Xu et al. (2012) extended here to include the quadrupole (see below). A detailed description of the method is given there. This method relies on a form of the Gaussian covariance matrix that includes some additional modification parameters. These allow us to

adjust the amount of shot-noise and sample variance to best match the covariances calculated directly from the mock correlation functions. To derive values for these modification parameters, we maximize the likelihood function

$$\mathcal{L} = \prod_{i=0}^N (2\pi)^{-q/2} (\det C)^{-1/2} \exp(-\chi_i^2/2). \quad (58)$$

Here  $N$  is the total number of mocks and  $q$  is the number of points to fit. We derive the parameters using the mock covariances between  $50 < r < 200h^{-1}\text{Mpc}$  (50 monopole points and 50 quadrupole points) and hence  $q = 50 \times 2 = 100$ .  $\chi_i^2 = \vec{x}_i^T C^{-1} \vec{x}_i$  where  $\vec{x}_i$  is a column vector of dimension  $q$  containing the difference between the monopole and quadrupole of each mock and the average of all mocks.  $C$  is the modified form of the Gaussian covariance matrix derived below and defined in Equation (62). We use this method since the mock covariances show evidence of noise and ideally the covariance matrix should be smooth.

The method allows us to include the redshift dependence of the galaxy number density  $\bar{n}$  assuming that it has no angular dependence. This is anchored in the observation that the covariance in configuration space is just the transform of the variance in Fourier space  $P_{\ell\ell'}^2(k)/V$ . Hence, we can imagine building up the inverse variance as

$$I^2(k) = \int \frac{dV}{P_{\ell\ell'}^2(k)} \quad (59)$$

where

$$dV = \frac{c}{H_0} \frac{R^2(z)}{\sqrt{\Omega_m(1+z)^3 + \Omega_\Lambda}} dz d\Omega \quad (60)$$

for a flat universe. Here,  $R(z)$  is the comoving distance to redshift  $z$ . We can then redefine the variance as  $\mathfrak{P}_{\ell\ell'}^2(k) = [I^2(k)]^{-1}$ .

Swapping this new expression for the variance into Equation (44) gives

$$C_{ij}(\xi_\ell(r_i), \xi_{\ell'}(r_j)) = 2(2\ell + 1)(2\ell' + 1) \cdot \int \frac{k^3 d\log(k)}{2\pi^2} \mathcal{J}_\ell(kr_i) \mathcal{J}_{\ell'}(kr_j) \mathfrak{P}_{\ell\ell'}^2(k). \quad (61)$$

We can then insert the modification parameters  $c_0$ ,  $c_1$ ,  $c_2$  and  $c_3$  such that

$$C_{ij}(\xi_\ell(r_i), \xi_{\ell'}(r_j)) = 2(2\ell + 1)(2\ell' + 1) \cdot \left[ \int \frac{k^3 d\log(k)}{2\pi^2} \mathcal{J}_\ell(kr_i) \mathcal{J}_{\ell'}(kr_j) \cdot \mathfrak{P}_{\ell\ell'}^2(k; c_0, c_1, c_2) \right] + c_3. \quad (62)$$

Here, where we have made the substitution

$$P(k, \mu) + \frac{1}{\bar{n}} \rightarrow \left[ c_0 P_{dw}(k, \mu) + \frac{c_1}{\bar{n}(z)} \right] (1 + \beta\mu^2)^2 F(k, \mu, \Sigma_s) + \frac{c_2}{\bar{n}(z)} \quad (63)$$

in Equation (34). The  $c_0$  term adjusts the magnitude of the sample variance. The  $c_1$  term acts like a non-linear shot-noise component and the  $c_2$  term adjusts the magnitude of the standard Poisson shot-noise contribution. The  $c_3$  term can be associated with the integral constraint, which appears as an additive offset in the correlation function.

In calculating the covariance matrix, we set  $\beta = f/b$  before reconstruction and  $\beta = 0$  after reconstruction, again due to the expected removal of large-scale redshift-space distortions. We test several cases where we vary  $\beta$  from these fiducial values and find that changing  $\beta$  affects the relative amplitudes of the  $C_{ij}(\xi_0(r_i), \xi_0(r_j))$  and  $C_{ij}(\xi_2(r_i), \xi_2(r_j))$  terms. This can cause slight changes in the resulting  $\sigma_\alpha$  and  $\sigma_\epsilon$  at the 0.1% level, which is not significant at our current levels of statistical precision. The  $\Sigma_s$  streaming scale for the FoG is fixed at  $4h^{-1}\text{Mpc}$ . We find very little difference in the resulting modification parameters in cases where we allow  $\Sigma_s$  to vary. We fix  $\Sigma_\perp$  and  $\Sigma_\parallel$  to their fiducial model values (recapped below) in our covariance matrix calculations. The modification parameters we obtain are  $c_0 = 1.06$ ,  $c_1 = 0.11$ ,  $c_2 = 1.49$ ,  $c_3 = 5.18 \times 10^{-8}$  before reconstruction, and  $c_0 = 1.12$ ,  $c_1 = 0.05$ ,  $c_2 = 1.58$ ,  $c_3 = 8.82 \times 10^{-8}$  after reconstruction. With these modification parameters in hand, we can construct a smooth approximation to the mock covariances from the binned Gaussian covariance matrix using Equation (62).

Our fiducial model parameters are summarized as follows: we define our fiducial model before reconstruction to have  $\Sigma_\perp = 6h^{-1}\text{Mpc}$ ,  $\Sigma_\parallel = 10h^{-1}\text{Mpc}$ ,  $\Sigma_s = 4h^{-1}\text{Mpc}$  and a prior on  $\beta$  centered on  $\beta = 0.35$ . After reconstruction, we set  $\Sigma_\perp = \Sigma_\parallel = 3h^{-1}\text{Mpc}$  and center our  $\beta$  prior on 0. Our fiducial fitting range is  $50 < r < 200h^{-1}\text{Mpc}$ .

In §5 and §6, we present our measured values of  $\alpha$  and  $\epsilon$  for the mocks (§4.1) and actual survey data (§4.2) using the fitting models defined in Equations (49) & (50) and the modified Gaussian covariance matrix described above.

## 4 DATASETS

### 4.1 Simulations

We use the Large Suite of Dark Matter Simulations (LasDamas; McBride et al. 2012, in prep) to calibrate and test our reconstruction parameters, fitting template and covariance matrix. The LasDamas collaboration<sup>1</sup> has provided publicly available mock galaxy catalogues based on these simulations for the Sloan Digital Sky Survey (SDSS) data release 7 (DR7) luminous red galaxy (LRG) sample. In particular, we use the "gamma" release mock catalogues referred to as **lrgFull**.

The LasDamas simulations were run assuming a flat  $\Lambda\text{CDM}$  cosmology with  $\Omega_b = 0.04$ ,  $\Omega_m = 0.25$ ,  $h = 0.7$ ,  $n_s = 1.0$  and  $\sigma_8 = 0.8$ . Although various box sizes were implemented, the 40 simulations used to construct the LRG mocks were  $2.4h^{-1}\text{Gpc}$  on a side with  $1280^3$  particles in each. The initial particle positions were set using second-order Lagrangian perturbation theory at  $z = 49$ . To construct mock galaxy catalogues from the simulations, the dark matter halos were populated according to halo occupation parameters tuned to match the observed clustering of the DR7 LRGs. In addition, the mock catalogues include observational effects such as redshift-space distortions and mimic the angular selection function of the LRG sample. The redshift range covered by the mocks is  $0.16 < z < 0.44$ . We note that this is slightly different to the flux-limited

<sup>1</sup> <http://lss.phy.vanderbilt.edu/lasdama>

LRG sample described in the following section that will be employed in this study. When fitting the data, we account for this by extrapolating our covariance matrix using the observed  $\bar{n}(z)$  and the formalism described in the previous section. In addition, we slightly downsample the  $\bar{n}(z)$  distribution in the mocks to better match the data. Our region of interest, the SDSS Northern Galactic Cap, covers  $\sim 7200 \text{ deg}^2$  on the sky. The resulting geometry allows 4 mocks to be constructed from each simulation and hence we have a total of 160 mocks for our analysis.

## 4.2 SDSS DR7

The observational dataset used in this study is the SDSS (York et al. 2000) DR7 (Abazajian et al. 2009) LRG sample. The same dataset was also used in the monopole-only BAO analysis of Padmanabhan et al. (2012), Xu et al. (2012) & Mehta et al. (2012).

The SDSS has taken photometric observations of  $\sim 10,000 \text{ deg}^2$  on the sky and obtained spectroscopic followup of nearly a million of these detected objects. It uses a dedicated 2.5m telescope (Gunn et al. 2006) at Apache Point Observatory which has a specially designed wide field camera (Gunn et al. 1998). Photometric observations were taken in the *ugriz* bands (Fukugita et al. 1996; Smith et al. 2002) by drift scanning the sky under favourable conditions (Hogg et al. 2001). These images were then fed through an automated pipeline that performed the necessary astrometric and photometric calibrations. The pipeline also detected and measured the photometric properties of the observed objects (Pier et al. 2003; Ivezić et al. 2004; Tucker et al. 2006; Padmanabhan et al. 2008). Select subsamples (Strauss et al. 2002; Eisenstein et al. 2001) were then designated for spectroscopic followup using a 640 fiber spectrograph.

The DR7 LRG sample is part of the last data release of SDSS-II, the second phase of SDSS which was completed in 2009. The LRG sample was selected according to the prescription in Eisenstein et al. (2001). This selection was optimized to identify the most luminous (and hence most massive and highly biased) galaxies which can be observed out to high redshifts. Since the volume encompassed by equal angles on the sky increases with redshift, we can probe the large volumes necessary for cosmological studies using these luminous galaxies. The LRGs tend to be old systems with uniform spectral energy distributions that exhibit a strong  $4000\text{\AA}$  break. This gives them a distinct colour-flux-redshift relation which allows them to be uniformly selected over a wide redshift range. Our sample matches exactly that of Kazin et al. (2010a) and we refer the interested reader there for details of its construction. We use the flux-limited LRG sample in the SDSS Northern Galactic Cap only. This sample spans a redshift range of  $0.16 < z < 0.47$  and has a number density of  $\sim 10^{-4} h^3 \text{ Mpc}^{-3}$ .

## 5 MOCK CATALOGUE RESULTS

In this section we present the results of fits to the LasDamas mock correlation functions before and after reconstruction. These were computed and fit by taking the LasDamas cosmology as the fiducial cosmology.

We plot the average monopole and quadrupole of the 160 mocks before reconstruction in Figure 4. The fiducial templates (solid lines in Figures 1(b) & 2) are shown as the grey dotted lines. The monopole and the quadrupole at large scales look similar to the fiducial templates. However, the small scales ( $r \lesssim 50h^{-1} \text{ Mpc}$ ) in the quadrupole show substantially different structure indicating that our model does not fit the data well at these scales. This motivates our choice for the fiducial fitting range:  $50 < r < 200h^{-1} \text{ Mpc}$ . The best-fit model to the monopole and quadrupole are overplotted as the red lines where the solid line corresponds to using the fiducial  $A_{0,2}(r)$  and the dashed line corresponds to using  $A_{0,2}(r) = 0$  (i.e. no broadband marginalization). The monopole fits look very similar; however the fiducial  $A_{0,2}(r)$  does much better in the quadrupole near the acoustic scale with  $\chi^2$  decreasing by  $\sim 33$  relative to the  $A_{0,2}(r) = 0$  fit. We allow  $\Sigma_{\perp}$  and  $\Sigma_{\parallel}$  to vary in these fits and obtain best-fit values of  $6.3h^{-1} \text{ Mpc}$  and  $10.4h^{-1} \text{ Mpc}$ , motivating our choices in the fiducial model. We keep  $\Sigma_s$  fixed at  $4h^{-1} \text{ Mpc}$ .

A comparison of the monopole and quadrupole before and after reconstruction is shown in Figure 5. As in Padmanabhan et al. (2012), we see the acoustic peak in the monopole appears less smeared after reconstruction which indicates that our reconstruction technique was effective at partially undoing non-linear evolution. This is also reflected in the fact that after reconstruction (where we assume the smearing is isotropic), a fit to the average of the mocks gave a much smaller BAO smoothing scale of  $\Sigma_{\text{nl}} = 2.9h^{-1} \text{ Mpc}$  as opposed to the pre-reconstruction values of  $\Sigma_{\perp} = 6.3h^{-1} \text{ Mpc}$  and  $\Sigma_{\parallel} = 10.4h^{-1} \text{ Mpc}$ . In addition, we see that the quadrupole is nearly zero on large scales after reconstruction, which implies that our reconstruction technique was also effective at partially removing the Kaiser effect. The fact that the quadrupole is positive and not exactly 0 is likely due to some slight anisotropy introduced by reconstruction. This is discussed in more detail below and shown not to significantly affect our measurements of  $\alpha$  and  $\epsilon$ .

By averaging the mocks we have effectively increased the survey volume by a factor of 160 and hence the variance should decrease by an equal amount. This means that the average of the mocks should have substantially less noise. In addition, we know that we are computing the correlation functions and fitting using the correct (LasDamas) cosmology. Hence, we expect that the  $\alpha$  and  $\epsilon$  values measured from the average of the mocks should be 1 and 0 respectively if our models are unbiased (i.e. there should be no shift in the location of the peak relative to the model and there should be no anisotropy). We find that fitting the pre-reconstruction mock average gives  $\alpha = 1.005$  and  $\epsilon = 0.003$  while post-reconstruction we measure  $\alpha = 1.002$  and  $\epsilon = 0.002$ . The slight offset in  $\alpha$  from 1 is not too concerning as we expect non-linear structure growth to shift the peak by  $\lesssim 0.5\%$  (Padmanabhan & White 2009; Mehta et al. 2011). The fact that  $\alpha$  moves closer to 1 after reconstruction is encouraging as reconstruction is supposed to remove some effects of non-linear structure growth. The small bias in  $\epsilon$  is not significant at our current levels of statistical precision and is likely the result of small mismatches between the broadband model and the data. This will be discussed in more detail shortly. We again emphasize that in these fits we have allowed  $\Sigma_{\parallel}$  and  $\Sigma_{\perp}$  to vary. When we fit the individual mocks,

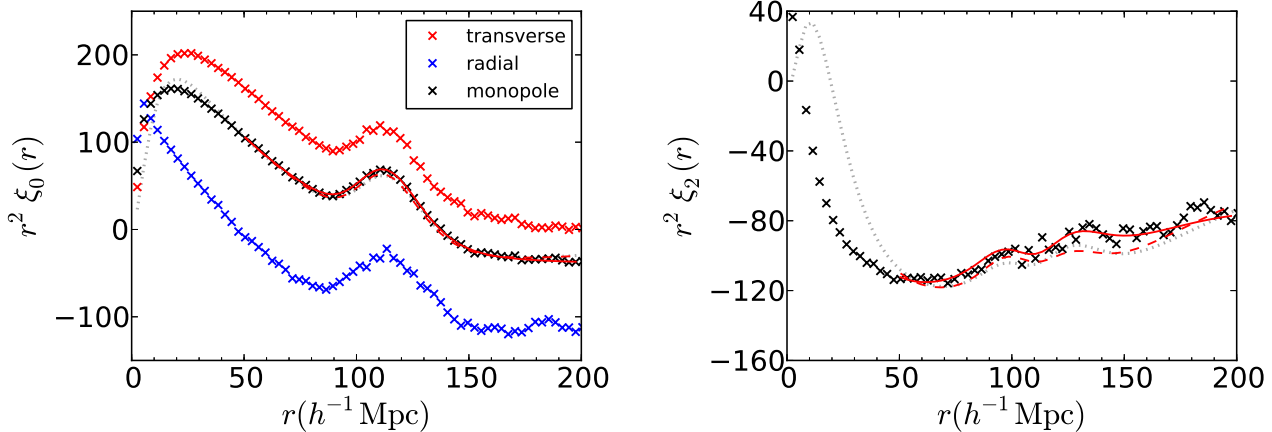


**Figure 4.** Average monopole (left) and quadrupole (right) of the 160 mock catalogues before reconstruction. The monopole and the quadrupole at large scales are similar to the fiducial templates (grey dotted lines, identical to the solid lines plotted in Figures 1(b) & 2). The quadrupole on small scales ( $r \lesssim 50h^{-1}\text{Mpc}$ ), however, shows substantially different structure to the fiducial template. The fit to the average of the monopole and quadrupole from the mocks is overplotted in red. The solid line corresponds to a fit using the fiducial  $A_{0,2}(r)$  (Equation (51)) and the dashed line corresponds to a fit using  $A_{0,2}(r) = 0$ . We allow  $\Sigma_{\perp}$  and  $\Sigma_{\parallel}$  to vary in these fits and obtain best-fit values of  $6.3h^{-1}\text{Mpc}$  and  $10.4h^{-1}\text{Mpc}$  respectively using the fiducial  $A_{0,2}(r)$ . In the monopole case, the fit using the fiducial  $A_{0,2}(r)$  is very similar to the  $A_{0,2}(r) = 0$  fit. In the quadrupole, the  $A_{0,2}(r) = 0$  fit is much worse around the acoustic scale. Overall,  $\chi^2$  decreased by  $\sim 33$  going from  $A_{0,2}(r) = 0$  to the fiducial  $A_{0,2}(r)$ .

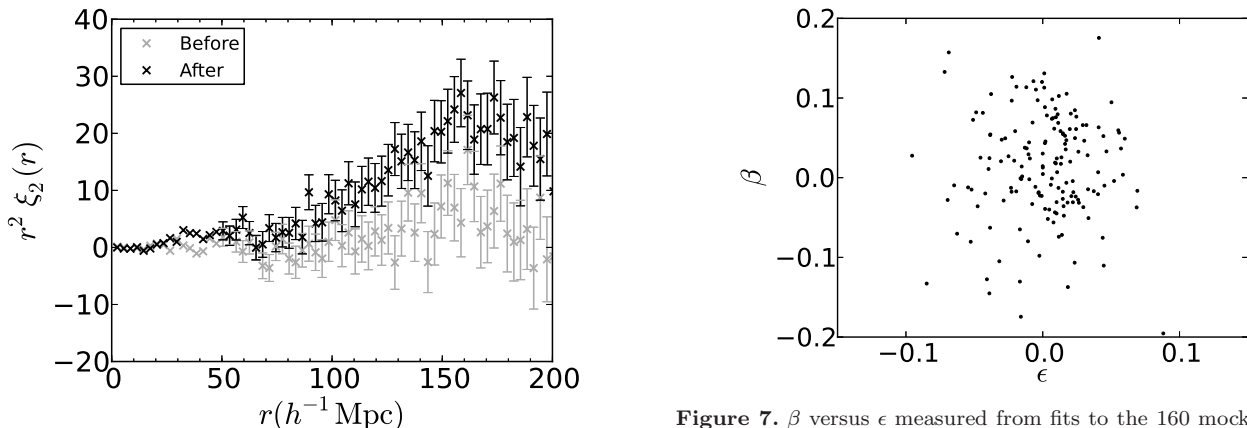


**Figure 6.** Average quadrupole from the mocks in real space before (grey) and after (black) reconstruction. The quadrupole before reconstruction is very close to 0 as we would expect in real space due to the lack of redshift-space distortions. Our  $\epsilon$  measurements are unbiased in this case which suggests that the small biases we see in redshift space are due to slight mismatches between our redshift-space distortion models and the actual broadband in the data. After reconstruction, the quadrupole at large scales acquires some additional power likely due to the survey geometry and sample number density fluctuations as a function of redshift. Our post-reconstruction real space  $\epsilon$  measurements remain unbiased which suggests that this anisotropy can be accounted for by our  $A_2(r)$  nuisance terms.

the signal-to-noise of the data is not sufficient for constraining any of these parameters and hence we fix them in the fiducial model to the values obtained in the averaged mock fits.

We measure  $\alpha$  and  $\epsilon$  for each mock using the fitting procedure and fiducial model outlined in §3.3. We also estimate

**Figure 7.**  $\beta$  versus  $\epsilon$  measured from fits to the 160 mocks after reconstruction. One can see that these two parameters are uncorrelated. We see similar results before reconstruction as well.

the errors  $\sigma_{\alpha}$ ,  $\sigma_{\epsilon}$  and the correlation coefficient  $\rho_{\alpha\epsilon}$  for each mock using Equations (55) & (57). Before reconstruction, we measure a mean  $\langle\alpha\rangle = 1.003 \pm 0.003$  with an rms scatter between the mocks of 0.034 and a median  $\tilde{\alpha} = 1.008$  with 16th/84th percentiles of the mocks corresponding to  ${}^{+0.030}_{-0.036}$  (these will henceforth be denoted the quantiles). For  $\epsilon$  we measure a mean  $\langle\epsilon\rangle = 0.001 \pm 0.003$  with an rms scatter between the mocks of 0.037 and a median  $\tilde{\epsilon} = 0.004$  with quantiles  ${}^{+0.032}_{-0.037}$ . After reconstruction, we measure a mean  $\langle\alpha\rangle = 1.002 \pm 0.002$  with an rms scatter between the mocks of 0.024 and a median  $\tilde{\alpha} = 1.002$  with quantiles  ${}^{+0.023}_{-0.022}$ . For  $\epsilon$  we measure a mean  $\langle\epsilon\rangle = 0.002 \pm 0.003$  with an rms scatter between the mocks of 0.032 and a median  $\tilde{\epsilon} = 0.007$  with quantiles  ${}^{+0.023}_{-0.037}$ . These values were calculated after rejecting the mocks where the acoustic signal is too weak to obtain an accurate centroiding of the BAO peak. This corresponds to

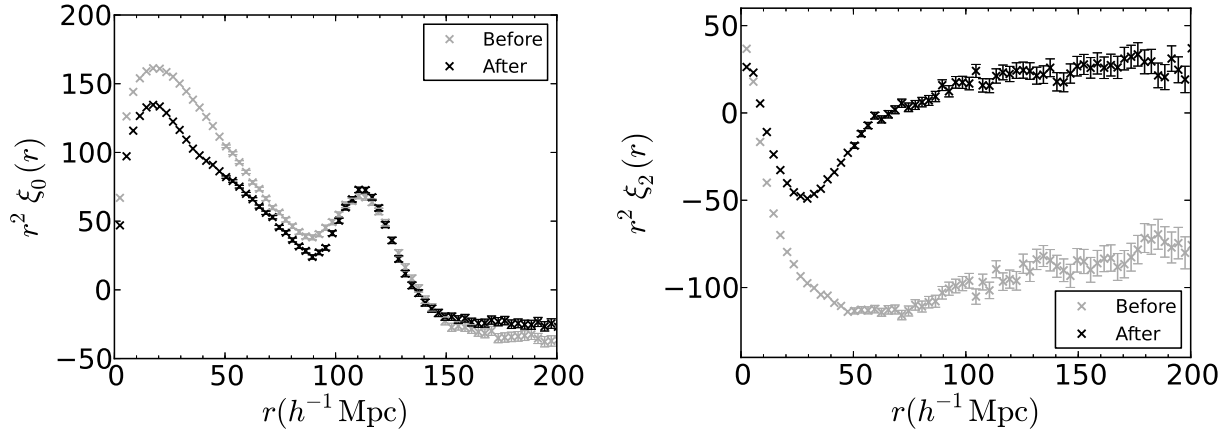


**Figure 5.** The average monopole (left) and quadrupole (right) of the 160 mocks before (gray crosses) and after (black crosses) reconstruction. One can see that after reconstruction, the acoustic peak in the monopole has sharpened up, indicating that reconstruction is effective at removing the degradation of the BAO caused by non-linear structure growth. In the quadrupole, the power at large-scales goes close to 0 which implies that reconstruction was effective at removing the Kaiser effect. It is not exactly zero due to some small anisotropy introduced by the reconstruction technique itself (see Figure 6). We note that the quadrupole is multiplied by  $r^2$  in this figure and hence the magnitude of this anisotropy is exaggerated.

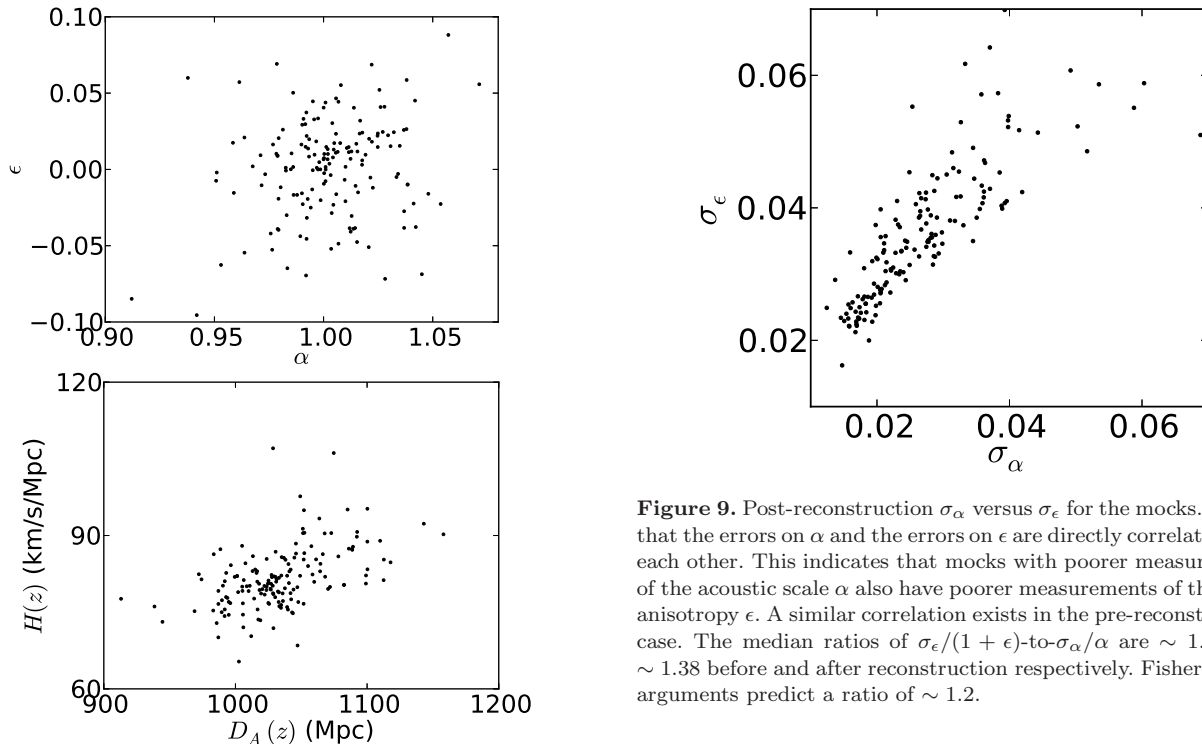


**Figure 8.**  $\alpha$  versus  $\epsilon$  (top) and  $D_A(z)$  versus  $H(z)$  (bottom) for the mocks after reconstruction. One can see that  $\alpha$  and  $\epsilon$  are not highly correlated. From the points plotted we measure a correlation coefficient of 0.27 and analogously in the pre-reconstruction case we measure 0.20. These are in excellent agreement with Fisher matrix predictions ( $\rho_{\alpha\epsilon} \sim 0.21$ ). We see a stronger correlation between  $D_A$  and  $H$  which we obtained by combining  $\alpha$  and  $\epsilon$  as in Equations (5) & (6). We expect  $\rho_{D_A H} \sim 0.4$  and we find correlation coefficients of 0.23 and 0.50 between our measured  $D_A$  and  $H$  values before and after reconstruction respectively.

**Figure 9.** Post-reconstruction  $\sigma_\alpha$  versus  $\sigma_\epsilon$  for the mocks. We see that the errors on  $\alpha$  and the errors on  $\epsilon$  are directly correlated with each other. This indicates that mocks with poorer measurements of the acoustic scale  $\alpha$  also have poorer measurements of the BAO anisotropy  $\epsilon$ . A similar correlation exists in the pre-reconstruction case. The median ratios of  $\sigma_\epsilon/(1 + \epsilon)$ -to- $\sigma_\alpha/\alpha$  are  $\sim 1.24$  and  $\sim 1.38$  before and after reconstruction respectively. Fisher matrix arguments predict a ratio of  $\sim 1.2$ .

making a cut in  $\sigma_\alpha$  at 0.07 and discarding the mocks that lie above this cut as demonstrated in Xu et al. (2012). Before reconstruction, 9 mocks out of 160 lie above this cut and after reconstruction, 0 lie above this cut.

The median  $\epsilon$  in the pre- and post-reconstruction cases are different from 0 and from the mean at  $\gtrsim 1$ -2 times the error on the mean. In addition, the post-reconstruction quantities are asymmetric, implying that the posterior  $\epsilon$  distribution deviates from Gaussian. These appear to be in part due to the intrinsic noise in the data and in part due to a slight mismatch between the model and the data. To reduce

**Table 1.**  $\epsilon$  statistics for various mock combinations. The first column indicates the number of mocks we have combined ( $m$ ). The second column quotes the mean  $\epsilon$  we measure with the standard error on the mean. The third column shows the rms of the mocks. The fourth column quotes the median  $\epsilon$  and the fifth column quotes the quantiles.

$m$	$\langle\epsilon\rangle$	rms	$\tilde{\epsilon}$	Qtls
Redshift Space without Reconstruction				
1	$0.001 \pm 0.003$	0.037	0.004	$+0.032$ $-0.037$
2	$0.001 \pm 0.003$	0.029	0.006	$+0.023$ $-0.030$
4	$0.001 \pm 0.003$	0.019	-0.001	$+0.017$ $-0.010$
8	$0.002 \pm 0.003$	0.012	0.002	$+0.009$ $-0.013$
Redshift Space with Reconstruction				
1	$0.002 \pm 0.003$	0.032	0.007	$+0.023$ $-0.037$
2	$0.003 \pm 0.002$	0.018	0.006	$+0.012$ $-0.020$
4	$0.003 \pm 0.002$	0.012	0.003	$+0.012$ $-0.011$
8	$0.003 \pm 0.002$	0.008	0.006	$+0.004$ $-0.007$

noise, we effectively increase the spatial volume of the data by combining our 160 mocks into groups of 2, 4 and 8, and re-perform our fits. In general, we see a better agreement between the mean and median  $\epsilon$ . The quantiles remain mildly asymmetric in some cases but overall we see improved agreement. The rms scatter decreases by roughly the expected amount ( $\sim \sqrt{m}$ , where  $m = 2, 4$  or  $8$ ) if we consider  $\epsilon$  to be Gaussian. These results are summarized in Table 1.

We see that there is a persistent bias in  $\epsilon$  towards non-zero values that is currently below our detection threshold. This bias is  $\lesssim 1\sigma$  significant before reconstruction and only at the  $1\text{--}1.5\sigma$  level after reconstruction. To further test this, we split the mocks into 2 groups of 80 which reduces the noise in the data. After re-performing the fits, we find  $\langle\epsilon\rangle \sim 0.002$  both before and after reconstruction. These values agree with the fit results to the average of the 160 mocks described above. This suggests that the persistent bias in  $\epsilon$  is not due to noise but is rather a result of some mismatch between the model and the data. In our fits we fix  $\Sigma_{\perp}$ ,  $\Sigma_{\parallel}$  and  $\Sigma_s$ , and use the nuisance terms in  $A_2(r)$  to account for any other mismatch in the broadband shape between the model and the data. However  $\Sigma_{\perp}$ ,  $\Sigma_{\parallel}$  and  $\Sigma_s$  are partially degenerate with  $\epsilon$ , so if they are fixed at non-optimal values that cannot be fully compensated by  $A_2(r)$  (see Figure 12(b)), the fitter can resort to adjusting  $\epsilon$ . We stress however, that such small biases in our redshift-space measurements of  $\epsilon$  are below the current detection limit in a single DR7 realization as indicated by the rms of the mocks.

We can gain additional insights by analyzing the real-space mocks which do not have redshift-space distortions and therefore do not require  $\Sigma_s$  or anisotropic  $\Sigma_{nl}$  in the model. We find that these give non-biased measures of  $\epsilon$  in both the pre- and post-reconstruction cases. In the pre-reconstruction case we measure the mean  $\epsilon$  to be  $\langle\epsilon\rangle = 0.003 \pm 0.003$  with an rms between the mocks of 0.037. The median is  $\tilde{\epsilon} = 0.002$  with quantiles  $^{+0.040}_{-0.040}$ . After reconstruction we measure  $\langle\epsilon\rangle = 0.001 \pm 0.002$  with a mock rms of 0.027 and  $\tilde{\epsilon} = -0.002$  with quantiles  $^{+0.030}_{-0.023}$ . One can see that the mean and median  $\epsilon$  are consistent with each other and with 0. Fitting the average of the 160 mocks gives  $\epsilon = 0.001$  and

0.000 before and after reconstruction respectively; again implying a largely unbiased measurement of  $\epsilon$  in real space.

An interesting artifact we do find is that reconstruction appears to introduce some broadband anisotropy as shown in Figure 6. Here we have plotted the mean of the real-space quadrupoles before (grey) and after (black) reconstruction. We see that the quadrupole is nearly 0 before reconstruction as expected since there should not be any anisotropies in real space. However, after reconstruction, the quadrupole acquires some additional large-scale power. The reconstruction displacement vectors may take on a subtle anisotropy due to the variation of number density with redshift or the survey geometry (i.e. if it is wider than it is deep). Fortunately, this broadband anisotropy introduced by reconstruction is fairly smooth and can be removed by the  $A_2(r)$  nuisance parameters as evidenced by our unbiased measures of  $\epsilon$  in post-reconstruction real space.

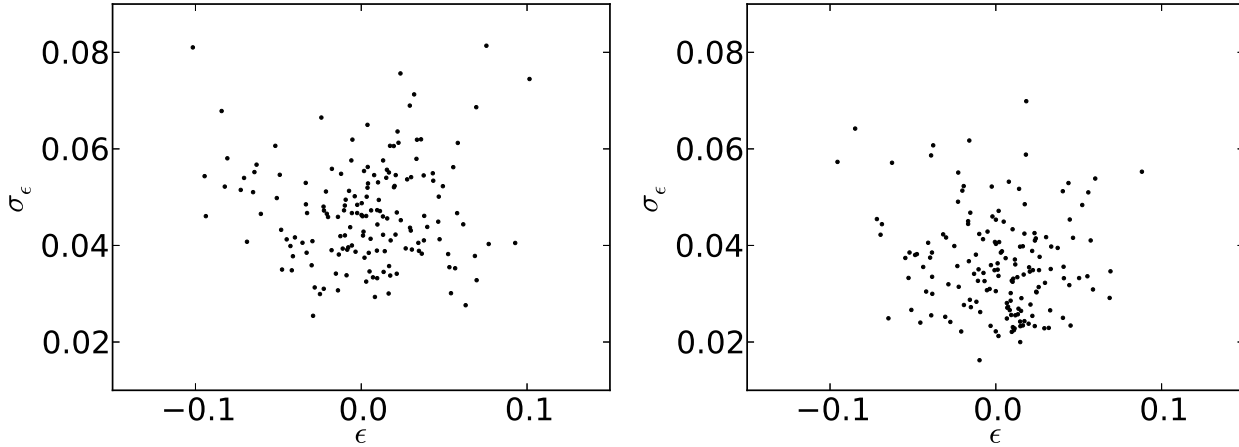
To build more intuition for the parameters we fit in redshift space and to demonstrate their inter-dependencies, we show various scatter plots of these quantities in Figures 7, 8, 9, 10 & 11. Figure 7 shows the values of  $\beta$  and  $\epsilon$  we obtain from our fits to the 160 mocks after reconstruction. Our pre-reconstruction results are similar. One can see that these two parameters are not correlated with each other.

The top panel of Figure 8 shows the  $\epsilon$  versus  $\alpha$  values we measure from the mocks after reconstruction. Again we see that these two parameters are not highly correlated. The correlation coefficient between  $D_A$  and  $H$  is predicted to be  $\rho_{D_A H} \sim 0.4$  (Seo & Eisenstein 2007). This subsequently predicts a  $\sigma_H/H$ -to- $\sigma_{D_A}/D_A$  ratio  $\sim 2$  (i.e. the fractional error of the Hubble parameter is twice that of the angular diameter distance). Using these values, a Fisher matrix argument shows that we should expect  $\rho_{\alpha\epsilon} \sim 0.21$  (see Appendix A). The correlation coefficient between the  $\alpha$  and  $\epsilon$  values plotted in Figure 8 is 0.20 and the corresponding pre-reconstruction value is 0.27. Both are in excellent agreement with the Fisher matrix prediction. The bottom panel of Figure 8 shows our  $\alpha$  and  $\epsilon$  measurements translated into measurements of  $D_A$  and  $H$  using Equations (5) & (6). In the plotted post-reconstruction case, the correlation coefficient between  $D_A$  and  $H$  is  $\sim 0.50$  and in the pre-reconstruction case it is  $\sim 0.23$ , which are not too different from our assumed  $\rho_{D_A H} = 0.4$ .

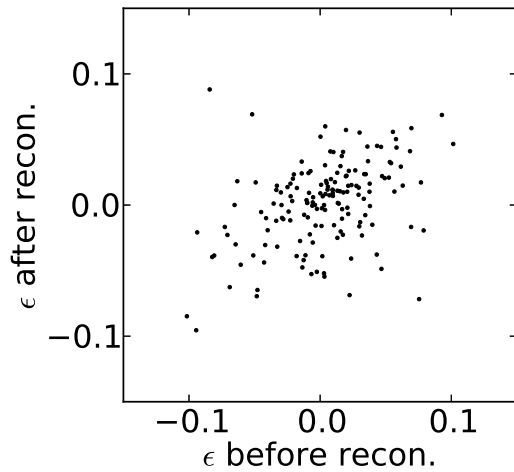
Figure 9 shows  $\sigma_{\epsilon}$  versus  $\sigma_{\alpha}$  for the mocks after reconstruction. We see that the errors on  $\alpha$  and  $\epsilon$  are correlated which implies that mocks with poorer measurements of the acoustic scale (i.e. larger  $\sigma_{\alpha}$  values) also have poorer measurements of the BAO anisotropy (i.e. larger  $\sigma_{\epsilon}$  values). We see a similar correlation in the pre-reconstruction results. Taking the ratio of  $\sigma_{\epsilon}/(1 + \epsilon)$ -to- $\sigma_{\alpha}/\alpha$ , we find a median  $\sim 1.24$  before reconstruction and  $\sim 1.38$  after reconstruction. Fisher matrix arguments predict a ratio of  $\sim 1.2$  (Equation A13), which is similar to what we see.

Figure 10 shows the values of  $\epsilon$  we measure versus  $\sigma_{\epsilon}$  before (left) and after (right) reconstruction. Reconstruction clearly decreases the scatter in  $\epsilon$  which is again highlighted in Figure 11, showing the values of  $\epsilon$  before and after reconstruction. While the two are correlated, the post-reconstruction values have smaller scatter as evidenced by the locus of points having a slope shallower than 1:1. From Figure 10 we also see that reconstruction decreases  $\sigma_{\epsilon}$ , our





**Figure 10.**  $\epsilon$  versus  $\sigma_\epsilon$  before (left) and after (right) reconstruction for the 160 mocks. One can see that reconstruction decreases the scatter in the measured  $\epsilon$  values (this is further highlighted in Figure 11). While reconstruction does decrease the average error on  $\epsilon$ , we see that the errors we measure are still fairly large compared to the errors on  $\alpha$  (see Figure 9).



**Figure 11.**  $\epsilon$  before reconstruction versus  $\epsilon$  after reconstruction fit from the 160 mocks. The slope of a linear fit to these points is less than 1 implying that the post-reconstruction  $\epsilon$  values have smaller scatter.

estimated error on  $\epsilon$ . However, these  $\sigma_\epsilon$  values are still large compared to  $\sigma_\alpha$  (see Figure 9).

Next we test the robustness of our fitting model to changes in various model parameters. A full list of these results are found in Table 2 for changes of  $\Sigma_\perp$ ,  $\Sigma_\parallel$ ,  $\Sigma_s$ , fitting range and form of  $A_2(r)$  both before and after reconstruction. In the table, *poly2* corresponds to an  $A_2(r) = a_1/r^2 + a_2/r$  and *poly4* corresponds to an  $A_2(r) = a_1/r^2 + a_2/r + a_3 + a_4r$ . We see that the scatter in  $\epsilon$  between the mocks can show  $\sim 10\%$  variations quite often. This again indicates the noisiness of our  $\epsilon$  measurements.

Figure 12 shows scatter plots in  $\alpha$  and  $\epsilon$  for a few sample cases. Here,  $\Delta\alpha$  and  $\Delta\epsilon$  are the differences between the  $\alpha$  and  $\epsilon$  values measured using the slightly altered model and the fiducial model. We expect the average  $\Delta\alpha$  and  $\Delta\epsilon$  to be 0 within the errors if our measurements of  $\alpha$  and  $\epsilon$  are consistent between the two models. We see that in all cases,  $\Delta\alpha = 0$  and  $\Delta\epsilon = 0$  fall within the scatter predicted by

the quantiles on a mock-by-mock basis. However, the errors on the average  $\Delta\alpha$  and  $\Delta\epsilon$  are on the order of  $\sqrt{160}$  times smaller than the scatter implied by the mocks. This indicates that in a few cases, we detect a significant shift in the average value of  $\alpha$  and  $\epsilon$  measured.

In particular, this occurs in the pre-reconstruction cases where we have changed the fitting range. The  $\alpha$  and  $\epsilon$  scatter plots for the  $30 < r < 200h^{-1}\text{Mpc}$  fitting range versus the fiducial fitting range cases are shown in Figure 12(a). The plots are shown in pairs with  $\alpha$  on the left and  $\epsilon$  on the right. The first plot in each pair corresponds to the pre-reconstruction case and the second plot to the post-reconstruction case. We see that on average, the larger fitting range gives slightly smaller values of  $\alpha$  and  $\epsilon$ . If we begin fitting at  $r = 30h^{-1}\text{Mpc}$  where the errorbars are smaller, the fitter forces the model to match the data at these small scales where we know the templates (especially the quadrupole) are not faithful representations of the data. The  $A_{0,2}(r)$  marginalization terms compensate for this at the expense of accurately fitting the BAO scale. After reconstruction,  $\Delta\alpha$  and  $\Delta\epsilon$  are both 0 which suggests that the model is better matched to the data in this case.

We also see average  $\Delta\epsilon$  values that are significantly different from zero in the  $\Sigma_s = 0h^{-1}\text{Mpc}$  case both before and after reconstruction. This is illustrated in Figure 12(b).  $\Sigma_s = 0h^{-1}\text{Mpc}$  implies that we exclude FoG from the model, which is unrealistic as it is implemented in the mocks. The likely culprit here is again the mismatch between the data and the model at small  $r$  especially in the quadrupole. In addition, if we compare the dotted line in Figure 2(b) (the  $\Sigma_s = 0h^{-1}\text{Mpc}$  case) and the average quadrupole in Figure 4, we see that the quadrupole BAO feature in this model is a poorer fit to the data overall. The mocks show more of a crest-trough-crest structure near the BAO scale as in the fiducial parameter template (solid lines in Figure 2) whereas the trough in the  $\Sigma_s = 0h^{-1}\text{Mpc}$  case is much weaker. This is further affirmed by the fact that the dotted line in Figure 2(a) (isotropic  $\Sigma_{\text{nl}}$ ) has a similar looking BAO feature and shows a similar discrepancy in  $\epsilon$  relative to the fiducial model before reconstruction. The fitter can

**Table 2.** Fitting results from the mocks for various models. The model is given in column 1. The median  $\alpha$  is given in column 2 with the 16th/84th percentiles from the mocks given in column 3 (these are denoted as the quantiles in the text, hence the label Qtls in the table). The median  $\epsilon$  is given in column 6 with corresponding quantiles in column 7. The median difference in  $\alpha$  on a mock-by-mock basis between the model listed in column 1 and the fiducial model is given in column 4 with corresponding quantiles in column 5. The analogues for  $\epsilon$  are given in columns 8 and 9. The mean  $\chi^2/\text{dof}$  is given in column 10.

Model	$\tilde{\alpha}$	Qtls	$\widetilde{\Delta\alpha}$	Qtls	$\tilde{\epsilon}$	Qtls	$\widetilde{\Delta\epsilon}$	Qtls	$\langle\chi^2\rangle/\text{dof}$
Redshift Space without Reconstruction									
Fiducial [ $f$ ]	1.008	+0.030 -0.036	–	–	0.004	+0.032 -0.037	–	–	92.01/90
Fit w/ $(\Sigma_{\perp}, \Sigma_{\parallel}) \rightarrow (8, 8)h^{-1}\text{Mpc}$ .	1.007	+0.029 -0.039	0.001	+0.003 -0.003	0.001	+0.032 -0.037	-0.002	+0.003 -0.003	92.06/90
Fit w/ $\Sigma_s \rightarrow 0h^{-1}\text{Mpc}$ .	1.005	+0.031 -0.037	-0.002	+0.002 -0.004	0.001	+0.031 -0.034	-0.003	+0.005 -0.004	91.85/90
Fit w/ $A_2(r) = \text{poly}2$ .	1.007	+0.031 -0.037	0.000	+0.002 -0.001	0.005	+0.032 -0.036	0.001	+0.005 -0.005	93.16/91
Fit w/ $A_2(r) = \text{poly}4$ .	1.006	+0.030 -0.035	0.000	+0.001 -0.001	0.002	+0.036 -0.034	-0.000	+0.007 -0.006	91.06/89
Fit w/ $30 < r < 200h^{-1}\text{Mpc}$ range.	1.003	+0.032 -0.037	-0.003	+0.004 -0.005	0.000	+0.032 -0.035	-0.003	+0.005 -0.005	106.04/104
Fit w/ $70 < r < 200h^{-1}\text{Mpc}$ range.	1.007	+0.029 -0.036	0.000	+0.002 -0.002	0.004	+0.032 -0.040	-0.000	+0.003 -0.003	79.39/76
Fit w/ $50 < r < 150h^{-1}\text{Mpc}$ range.	1.005	+0.030 -0.041	-0.000	+0.004 -0.006	0.004	+0.036 -0.043	-0.001	+0.008 -0.007	54.37/58
Redshift Space with Reconstruction									
Fiducial [ $f$ ]	1.002	+0.023 -0.022	–	–	0.007	+0.023 -0.037	–	–	92.68/90
Fit w/ $(\Sigma_{\perp}, \Sigma_{\parallel}) \rightarrow (2, 4)h^{-1}\text{Mpc}$ .	1.002	+0.023 -0.021	-0.000	+0.001 -0.001	0.008	+0.022 -0.037	0.000	+0.001 -0.001	92.73/90
Fit w/ $\Sigma_s \rightarrow 0h^{-1}\text{Mpc}$ .	1.001	+0.024 -0.020	-0.001	+0.005 -0.003	0.004	+0.020 -0.030	-0.003	+0.007 -0.005	92.27/90
Fit w/ $A_2(r) = \text{poly}2$ .	1.002	+0.024 -0.022	0.000	+0.001 -0.000	0.008	+0.023 -0.037	0.001	+0.002 -0.002	94.23/91
Fit w/ $A_2(r) = \text{poly}4$ .	1.002	+0.023 -0.022	0.000	+0.001 -0.001	0.005	+0.025 -0.037	-0.001	+0.004 -0.004	91.68/89
Fit w/ $30 < r < 200h^{-1}\text{Mpc}$ range.	1.003	+0.022 -0.023	0.000	+0.002 -0.001	0.006	+0.022 -0.038	0.000	+0.002 -0.002	106.12/104
Fit w/ $70 < r < 200h^{-1}\text{Mpc}$ range.	1.002	+0.023 -0.021	0.000	+0.001 -0.001	0.006	+0.022 -0.036	-0.000	+0.002 -0.002	79.99/76
Fit w/ $50 < r < 150h^{-1}\text{Mpc}$ range.	1.002	+0.024 -0.023	-0.001	+0.004 -0.004	0.008	+0.022 -0.037	-0.001	+0.005 -0.005	54.65/58
Recon. w/ $\beta \rightarrow 0.24$ .	1.002	+0.023 -0.022	-0.000	+0.001 -0.001	0.005	+0.023 -0.033	0.000	+0.002 -0.003	92.49/90
Recon. w/ $\beta \rightarrow 0.36$ .	1.002	+0.022 -0.020	0.000	+0.001 -0.002	0.005	+0.024 -0.038	-0.000	+0.002 -0.002	92.89/90
Recon. w/ $b \rightarrow 1.8$ .	1.001	+0.022 -0.021	-0.000	+0.006 -0.005	0.006	+0.025 -0.041	-0.000	+0.006 -0.006	92.61/90
Recon. w/ $b \rightarrow 2.6$ .	1.003	+0.023 -0.023	0.001	+0.004 -0.004	0.004	+0.025 -0.036	-0.001	+0.006 -0.005	92.65/90
Recon. w/ Wiener Filter.	1.004	+0.020 -0.022	-0.000	+0.004 -0.003	0.005	+0.024 -0.035	-0.000	+0.004 -0.004	92.69/90
Recon. on $\Omega_m = 0.4$ case. <sup>1</sup>	0.832	+0.021 -0.019	-0.171	+0.010 -0.010	0.020	+0.028 -0.037	0.017	+0.014 -0.014	92.61/90

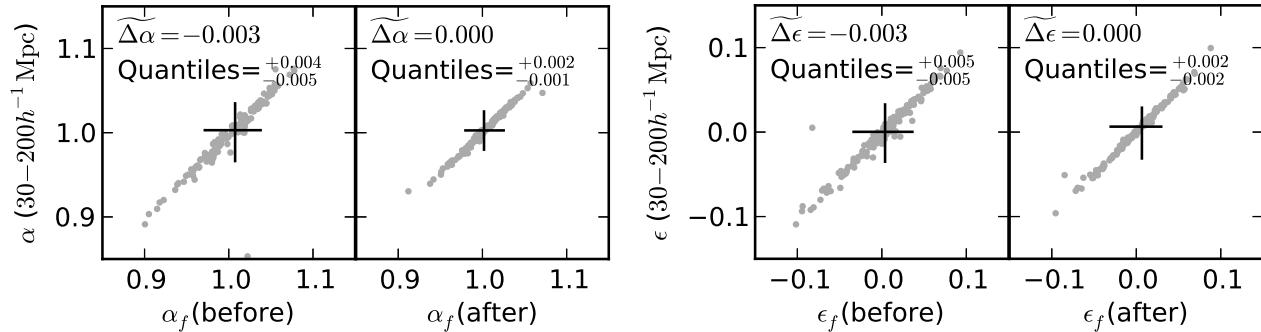
<sup>1</sup>  $\alpha = 1$  and  $\epsilon = 0$  in the LasDamas cosmology correspond to  $\alpha = 0.832$  and  $\epsilon = 0.013$  in this  $\Omega_m = 0.4$  cosmology according to Equations (5 & 6).

partially compensate for these differences through adjusting the value of  $\epsilon$  which also gives rise to crests and troughs near the BAO scale, although with different structure than those introduced through  $\Sigma_{\perp}$ ,  $\Sigma_{\parallel}$  and  $\Sigma_s$ . Hence one must pick a quadrupole model that has a BAO feature fairly well matched to the data to avoid biasing the  $\epsilon$  values measured.

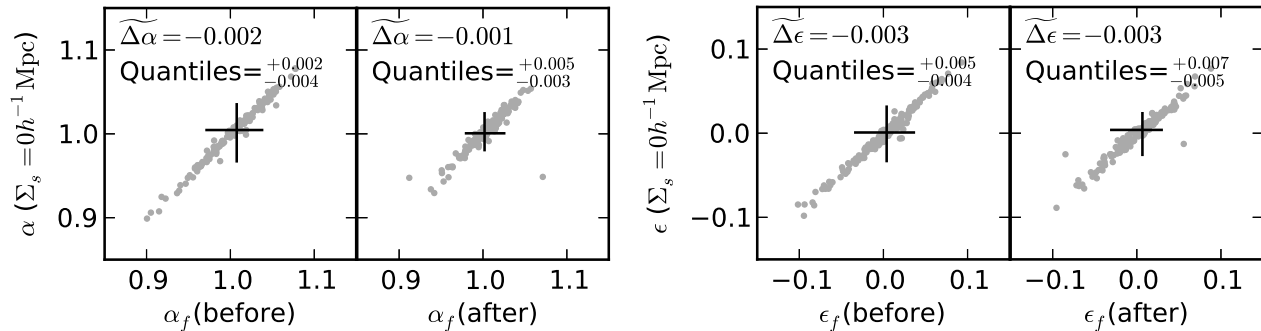
Despite these offsets in the median  $\alpha$  and  $\epsilon$  for different fitting models, we note that at the statistical precision of current datasets, we would not be able to detect any of these changes. For the DR7 mocks, the average  $\sigma_{\alpha}$  is  $\sim 0.04$  before reconstruction and  $\sim 0.03$  after reconstruction. The average  $\sigma_{\epsilon}$  are even larger at  $\sim 0.05$  before reconstruction and  $\sim 0.04$  after reconstruction. Hence, assuming that  $\sigma_{\alpha}$  and  $\sigma_{\epsilon}$  characterize the error on  $\alpha$  and  $\epsilon$ , a 0.003 shift will fall entirely within the expected errors. Therefore, our fitting

model is reasonably robust against small changes to model parameters and our measured  $\alpha$  and  $\epsilon$  values are largely unbiased.

We perform similar exercises for various different reconstruction parameters such as the bias and  $\beta$  values we input to the algorithm. The fiducial reconstruction parameters we use are  $b = 2.2$  and  $\beta = 0.3$ . We also tested using simple Wiener filtering to interpolate between masked regions. This differs from the constrained Gaussian realizations in that unobserved modes are set to 0 instead of being drawn from a fiducial power spectrum. Table 2 shows the results of these tests. It indicates that the unobserved modes do not affect our measurements of  $\alpha$  and  $\epsilon$  given our statistical precision, and that our fitting model effectively marginalizes away any broadband signal that reconstruction introduces



(a) Comparison of results obtained using a larger fitting range ( $30 < r < 200 h^{-1} \text{Mpc}$ ) versus the fiducial fitting range. Here, we see an average  $\Delta\alpha$  that is  $\sim -0.003$  before reconstruction. The error on the mean is a factor of  $\sim \sqrt{160}$  smaller than the scatter indicated by the quantiles, which makes this 0.003 shift statistically significant. This is caused by the templates being poor matches to the data at low  $r$ . While the  $A_{0,2}(r)$  terms attempt to compensate for this, accurate fitting of the BAO scale is compromised. The significant  $\Delta\epsilon$  in this case is rooted in the same cause. The fact that  $\Delta\alpha$  and  $\Delta\epsilon$  are both 0 after reconstruction suggests that the post-reconstruction model is better matched to the data.



(b) Comparison of results obtained using  $\Sigma_s = 0 h^{-1} \text{Mpc}$  versus the fiducial value of  $\Sigma_s = 4 h^{-1} \text{Mpc}$ . Here, we see that the average  $\Delta\epsilon$  is different from 0 when considering the error on the mean which is a factor of  $\sim \sqrt{160}$  smaller than the scatter indicated by the quantiles. This is caused by the quadrupole model being a less optimal match to the data. We note that these small shifts in  $\alpha$  and  $\epsilon$  are certainly not detectable in each mock, which have much larger errors on  $\alpha$  and  $\epsilon$  than  $\sim 0.003$ .

**Figure 12.** The robustness of our fitting model as demonstrated by  $\alpha$  and  $\epsilon$  scatter plots for some sample cases. Results for other changes to the fiducial model are given in Table 2. The plotted  $\alpha$  and  $\epsilon$  values were obtained through fitting the mock correlation functions before and after reconstruction. The plots are presented in pairs:  $\alpha$  on the left and  $\epsilon$  on the right. The first plot in each pair shows the pre-reconstruction results and the second plot shows the post-reconstruction results. The black crosses indicate the medians and quantiles of the mock measurements. If we obtain consistent measurements of  $\alpha$  and  $\epsilon$  with a model that has parameters slightly different to the fiducial model, then we should see  $\Delta\alpha$  and  $\Delta\epsilon$  values that are  $\sim 0$ . We see that this is true at the level of our current statistical precision. Therefore, our fitting model is reasonably robust against small changes to the fiducial model parameters.

when incorrect values of the fiducial parameters are used. Higher precision studies of possible systematics from reconstruction due to survey boundaries will be necessary for future surveys. However, this goes beyond the scope and goals of this current paper.

Finally we calculate and perform our fits using a fiducial cosmology that is significantly different to the LasDamas cosmology. This forces a stronger anisotropic BAO signal to appear in the quadrupole. We pick a cosmology with  $\Omega_m = 0.4$  that preserves the matter-to-baryon ratio of LasDamas. We also fix  $\Omega_m h^2$  which implies  $h = 0.553$ . We convert the measured  $\alpha$  and  $\epsilon$  values to  $D_A(z)$  and  $H(z)$  using Equations (5) & (6) and compare these to the values measured using the fiducial cosmology. This is illustrated in Figure 13. The equations listed above only allow us to infer  $D_A(z)/r_s$  and  $H(z)r_s$ . We have assumed  $r_s = 159.71 \text{ Mpc}$ , which is the sound horizon in the LasDamas cosmology, to

obtain the  $D_A(z)$  and  $H(z)$  values plotted in the figure. In the LasDamas cosmology (which is the true cosmology in our mocks),  $D_A(z) = 1032 \text{ Mpc}$  and  $H(z) = 81.8 \text{ km/s/Mpc}$  at  $z = 0.35$ . Taking the ratio  $\widehat{D_A}/D_A(z)$  and  $\widehat{H}/H(z)$  implies that on average our measurements of  $D_A(z)$  and  $H(z)$  using the  $\Omega_m = 0.4$  cosmology and the true LasDamas cosmology differ by  $\sim 0.7\%$  and  $\sim 0.6\%$  respectively. Dividing the scatter indicated by the quantiles by  $\sqrt{160}$  suggests that these average offsets are significant, although again, in a single mock, we would not be able to detect these offsets. The fiducial  $D_A(z)$  and  $H(z)$  are calculated assuming a median redshift of  $z = 0.35$ ; however, if the true median redshift were slightly different, such discrepancies would not be unexpected. In addition, our models for  $\alpha$  and  $\epsilon$  are based on Taylor expansions around 1 and 0 respectively. When the fitting model is constructed using a fiducial cosmology that is extremely wrong, the  $\alpha$  and  $\epsilon$  values we measure will de-

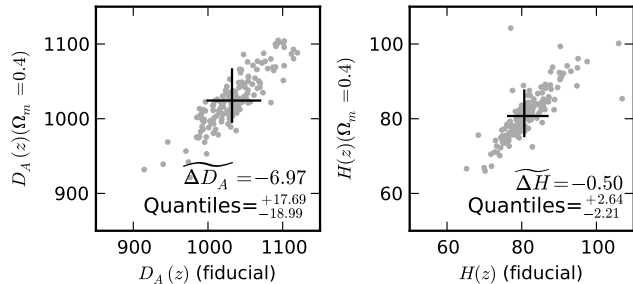


**Figure 13.**  $D_A(z)$  and  $H(z)$  scatter plots obtained by plotting those measured using an  $\Omega_m = 0.4$  cosmology versus the true LasDamas cosmology.  $D_A(z)$  is in units of Mpc and  $H(z)$  is in units of km/s/Mpc. These values were calculated using Equations (5) & (6) and assuming  $r_s = 159.71$  Mpc. The median  $\Delta D_A$  and  $\Delta H$  values are significantly different from 0 when approximating the error on the median as the scatter predicted by the quantiles divided by  $\sqrt{160}$ . Such a discrepancy may be due to our median redshift not being exactly  $z = 0.35$  as assumed. It could also be due to the breakdown of Taylor assumptions made in deriving our fitting model; in the  $\Omega_m = 0.4$  cosmology, our measured  $\alpha$  and  $\epsilon$  values deviate substantially from 1 and 0 as shown in the last row of Table 2. We again emphasize that while this difference is detectable in the median  $\alpha$  and  $\epsilon$  of the mocks, it is not significant in each individual mock.

viate significantly from 1 and 0 as shown in the last row of Table 2. Our first-order Taylor assumption may be breaking down at this point, further affecting our measurements. In this case, one can iteratively change the fiducial cosmology and re-fit for  $\alpha$  and  $\epsilon$  until values closer to 1 and 0 are obtained.

We verify our assumption that the second moments of  $p(\alpha)$  and  $p(\epsilon)$  are good indicators of the errors on  $\alpha$  and  $\epsilon$  in Figure 14. The top panel of this figure shows a normalized histogram of  $(\alpha - \langle \alpha \rangle) / \sigma_\alpha$  after reconstruction and the bottom panel shows the analogue for  $\epsilon$ . The unit normal is overplotted. We perform K-S tests on these distributions and list the p-values in the plots. These give the probability that the plotted distribution is drawn from a unit normal. One can see that the post-reconstruction p-values are 0.50 and 0.17 for  $\alpha$  and  $\epsilon$  respectively. For comparison, the corresponding pre-reconstruction p-values are 0.40 and 0.19. These values indicate that there are finite probabilities that  $\alpha$  and  $\epsilon$  have Gaussian posteriors. Hence the standard deviations  $\sigma_\alpha$  and  $\sigma_\epsilon$  we calculate from  $\chi^2(\alpha, \epsilon)$  characterize the errors on  $\alpha$  and  $\epsilon$  reasonably well.

## 6 DR7 RESULTS

### 6.1 Anisotropic Results

Now that we have verified the robustness of our techniques and obtained a better understanding of the anisotropic signal from our mocks, we can proceed to the actual SDSS DR7 LRG data. To calculate our fitting model for the data, we use the flat  $\Lambda$ CDM cosmology predicted by WMAP7:  $H_0 = 70.2 \pm 1.4$  km/s/Mpc,  $\Omega_b h^2 = 0.02255 \pm 0.054$ ,  $\Omega_c h^2 = 0.1126 \pm 0.0036$ ,  $n_s = 0.968 \pm 0.012$  and  $\sigma_8 = 0.816 \pm 0.024$  (Komatsu et al. 2011). For the covariance matrix, we again use the modified Gaussian covariance matrix discussed in

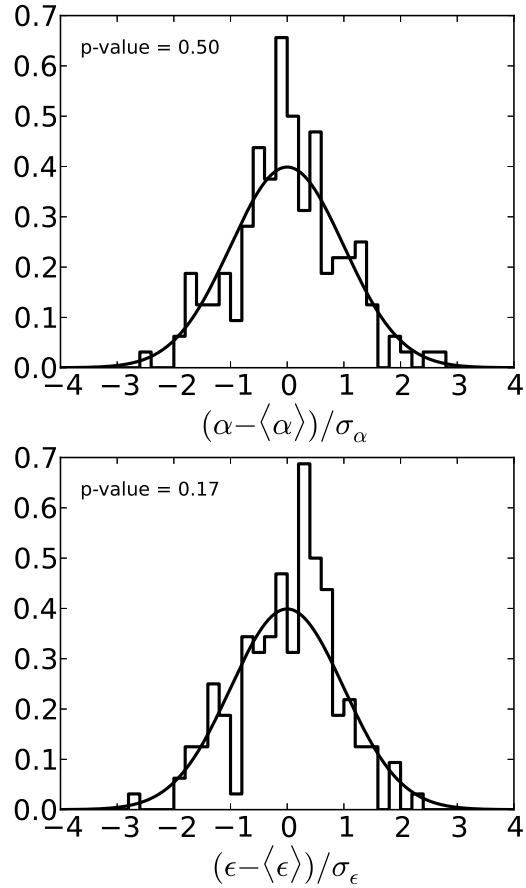


**Figure 14.** Histograms of  $(\alpha - \langle \alpha \rangle) / \sigma_\alpha$  (top) and  $(\epsilon - \langle \epsilon \rangle) / \sigma_\epsilon$  (bottom) after reconstruction. These are a measure of the signal-to-noise of our measured  $\alpha$  and  $\epsilon$  values. The overplotted black lines correspond to the unit normal. We perform a K-S test to see how likely these distributions are drawn from a unit normal distribution. The p-values or probabilities are indicated on the plots and imply that  $\alpha$  and  $\epsilon$  both have finite chances of being drawn from Gaussian distributions. This verifies that the standard deviations  $\sigma_\alpha$  and  $\sigma_\epsilon$  we calculate from  $\chi^2(\alpha, \epsilon)$  characterize the errors on  $\alpha$  and  $\epsilon$  reasonably well. A similar conclusion holds for our  $\alpha$  and  $\epsilon$  values before reconstruction.

§3.3 with the modification parameters derived from the mocks and the WMAP7 cosmology.

The results of our fits are shown in Figure 15. The pre-reconstruction results are in the top row and the post-reconstruction results are in the bottom row. The acoustic peak appears much sharper after reconstruction, again indicating the effectiveness of our technique in undoing non-linear evolution. This is reflected in the decrease in error on  $\alpha$  and  $\epsilon$  by factors of 1.8 and 1.3 respectively after reconstruction. The quadrupole near  $100h^{-1}$  Mpc scales is much closer to 0 after reconstruction which implies that our partial removal of the Kaiser effect was also successful. The deviation from 0 at larger scales again indicates that reconstruction is introducing some additional anisotropy. This is as expected based on our analysis of the mock catalogues in §5 (see Figure 6).

The first column of Figure 16 shows the  $\Delta\chi^2(\alpha, \epsilon) = \chi^2(\alpha, \epsilon) - \chi^2_{min}$  distribution measured at various grid points

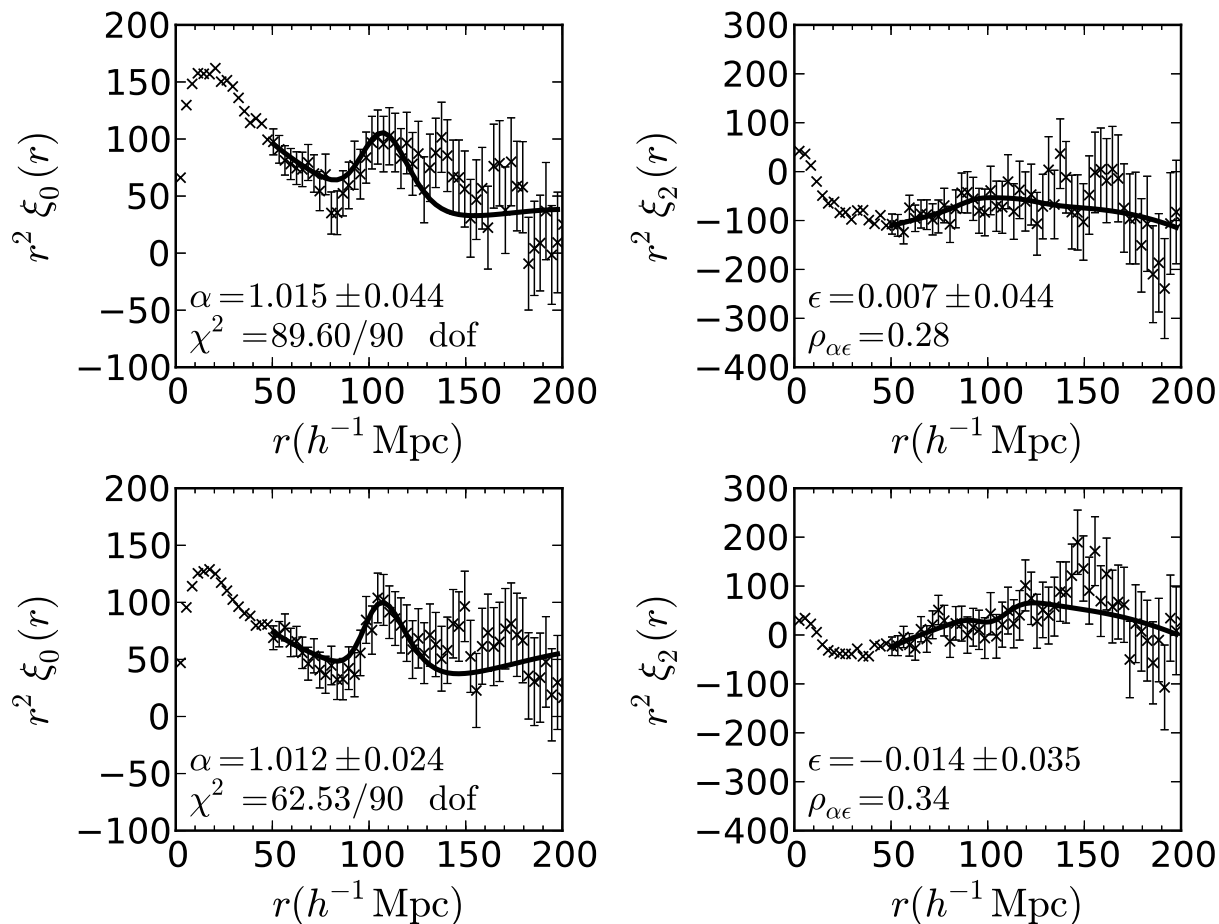


**Figure 15.** DR7 fit results before (top row) and after (bottom row) reconstruction. These values imply a 3.6% measurement of  $D_A(z)$  and an 8.3% measurement of  $H(z)$  after reconstruction. We see that the acoustic peak has sharpened up significantly after reconstruction as expected. The error on  $\alpha$  decreases by a factor of 1.8 and the error on  $\epsilon$  decreases by a factor of 1.3 as a result. The quadrupole is nearly 0 at  $\sim 100h^{-1}\text{Mpc}$  after reconstruction, indicating the effectiveness of our Kaiser correction. The deviation from 0 at larger  $r$  is likely some anisotropy introduced by reconstruction.

in  $\alpha$  and  $\epsilon$ . As described in §3.3, our  $\alpha$  grid points are separated by 0.0025 in the range  $0.7 < \alpha < 1.3$  and our  $\epsilon$  grid points are separated by 0.005 in the range  $-0.3 < \epsilon < 0.3$ . The 1 through  $6\sigma$  confidence levels for a 2D distribution are overplotted. The pre-reconstruction results are shown in the top row and the post-reconstruction results are shown in the bottom row. As we go to smaller  $\alpha$ , the acoustic peak in the model is being pushed out to larger scales where the errorbars are larger. Hence it is much easier for the fitter to hide the peak within the errors. Although we have applied a 0.15 prior in  $\log(\alpha)$  to suppress this unphysical downturn in  $\chi^2$ , the distribution still plateaus in this region. One can also see that after reconstruction, the  $\chi^2(\alpha, \epsilon)$  distribution is much tighter at the center, indicating that the best-fit values are much better measured. This corresponds to the smaller errorbars we see in  $\alpha$  and  $\epsilon$  after reconstruction.

The second and third columns of Figure 16 show the  $\alpha$  and  $\epsilon$  probability distributions derived from the  $\chi^2$  grid. One can see that both of these are fairly Gaussian so we can quantify the errors on  $\alpha$  and  $\epsilon$  as the second moments of these distributions,  $\sigma_\alpha$  and  $\sigma_\epsilon$ . These values are summarized in Table 3 for both before (top row) and after (bottom

row) reconstruction. The smaller standard deviations after reconstruction accompany the sharpening up of the acoustic peak. This corresponds to the tightening of the contours in the  $\chi^2$  distribution shown in column 1.

Our measured  $C_{\alpha\epsilon}$ ,  $\sigma_\alpha$  and  $\sigma_\epsilon$  imply correlation coefficients of  $\rho_{\alpha\epsilon} = 0.28$  and  $0.34$  before and after reconstruction. These values are slightly larger than the expected  $\rho_{\alpha\epsilon} \sim 0.21$  from Fisher matrix arguments. However, given the large rms of  $\rho_{\alpha\epsilon}$  from the mocks of  $\sim 0.35$  both before and after reconstruction, our DR7 results are not significantly different from the Fisher matrix prediction.

Using our measured  $\alpha$ ,  $\sigma_\alpha$ ,  $\epsilon$ ,  $\sigma_\epsilon$  and  $C_{\alpha\epsilon}$  values from the DR7 data, we can use Equations (5), (6), (8) & (9) to determine  $D_A(z = 0.35)$  and  $H(z = 0.35)$ . These results are again summarized in Table 3. In addition, Figure 17 shows the post-reconstruction  $\Delta\chi^2(D_A, H) = \chi^2(D_A, H) - \chi^2_{min}$  contour plot obtained from the  $\alpha$ - $\epsilon$  grid in Figure 16. The values listed in the table and plotted in the figure were obtained assuming  $r_s = 152.76$  Mpc and using the fiducial WMAP7 values:  $D_{A,f}(z = 0.35)/r_{s,f} = 6.69$  and  $H_f(z = 0.35)r_{s,f} = 12689$  km/s. We see that post-reconstruction we have a  $\sim 3.6\%$  measurement of  $D_A(z)$  and  $\sim 8.3\%$  measure-

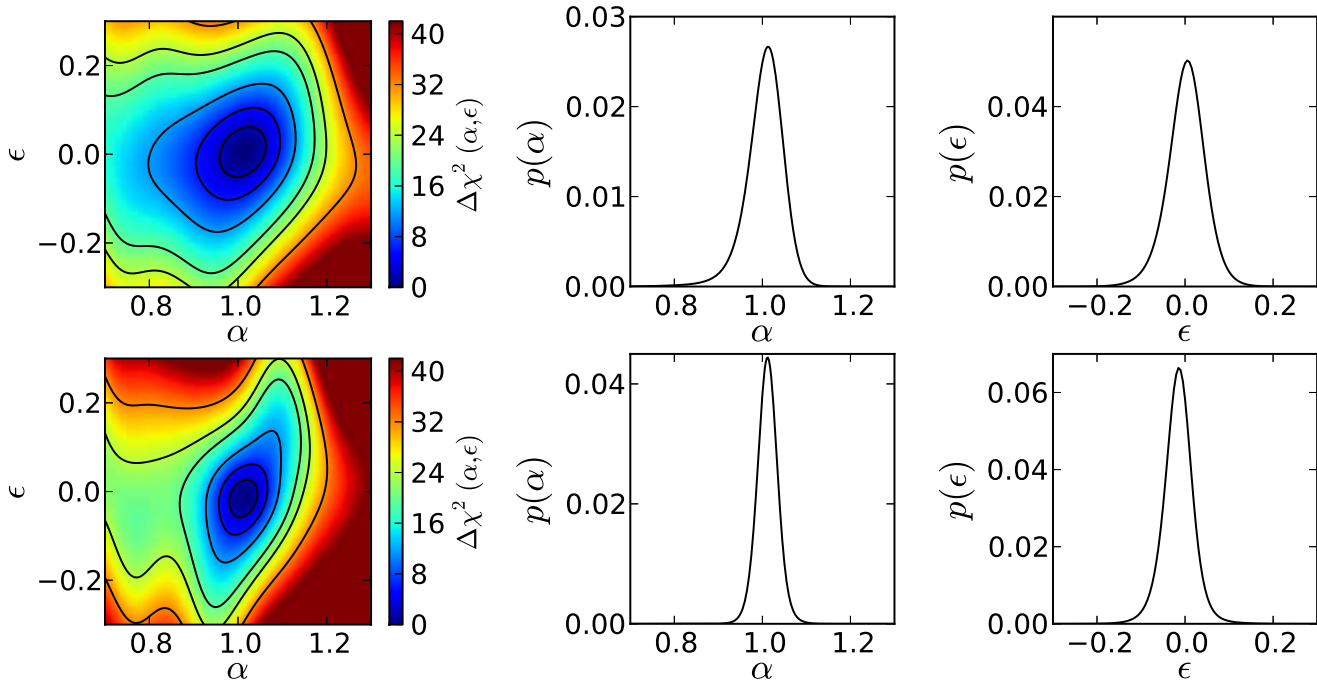


**Figure 16.** The  $\Delta\chi^2(\alpha, \epsilon)$  distribution (column 1) and the derived  $p(\alpha)$  and  $p(\epsilon)$  distributions (columns 2 & 3) for DR7. The pre-reconstruction results are in the top row and the post-reconstruction results are in the bottom row. Contour levels corresponding to 1-6 $\sigma$  for a 2D distribution are overplotted. We apply a 0.15 prior in  $\log(\alpha)$  to suppress the unphysical downturn at low  $\alpha$  which corresponds to the acoustic peak being pushed out to large  $r$ . The errorbars are much larger here and the fitter has an easier time hiding the peak inside the errors. The plateauing of the distribution at small  $\alpha$  is a result of this. We see that after reconstruction, the contours become much tighter. This corresponds to the tightening of  $p(\alpha)$  and  $p(\epsilon)$  after reconstruction seen in columns 2 & 3 due to the sharpening up of the acoustic peak. We also see that  $p(\alpha)$  and  $p(\epsilon)$  are nearly Gaussian and hence the second moments  $\sigma_\alpha$  and  $\sigma_\epsilon$  characterize the errors on  $\alpha$  and  $\epsilon$  well.

**Table 3.** Summary of key measurements from DR7 data. Columns 2 and 3 list the  $\alpha$  and  $\epsilon$  values we measure. Column 4 lists the covariance between  $\alpha$  and  $\epsilon$  while column 5 lists their correlation coefficient. Columns 6 and 7 list the distance constraints we obtain to  $z = 0.35$  from our measured  $\alpha$  and  $\epsilon$  values. Columns 8 and 9 translate these relative distance measures into more tangible quantities assuming  $r_s = 152.76$  Mpc as in the WMAP7 cosmology. The pre-reconstruction results are listed in the top row (Before) and the post-reconstruction results are listed in the bottom row (After).

	$\alpha$	$\epsilon$	$C_{\alpha\epsilon}$	$\rho_{\alpha\epsilon}$	$D_A(z)/r_s$	$H(z)r_s$ (km/s)	$D_A(z)$ (Mpc)	$H(z)$ (km/s/Mpc)	$\rho_{D_A H}$
Before	$1.015 \pm 0.044$	$0.007 \pm 0.044$	0.00054	0.28	$6.751 \pm 0.352$	$12339 \pm 1330$	$1031 \pm 54$	$80.8 \pm 8.7$	0.26
After	$1.012 \pm 0.024$	$-0.014 \pm 0.035$	0.00029	0.34	$6.875 \pm 0.246$	$12895 \pm 1070$	$1050 \pm 38$	$84.4 \pm 7.0$	0.57

ment of  $H(z)$  from SDSS DR7. Note that our measures of  $D_A$  and  $H$  are correlated; this is also clearly evident from the contour plot. Before reconstruction,  $\rho_{D_A H} = 0.26$  and after reconstruction  $\rho_{D_A H} = 0.57$ . These are similar to the  $\rho_{D_A H} \sim 0.4$  predicted by Seo & Eisenstein (2007).

We see that our DR7  $\sigma_\alpha$  and  $\sigma_\epsilon$  measurements fall nicely within the locus of mock points as shown in Figure 18 for the post-reconstruction case. Note that the mock results shown in this figure are identical to Figure 9. The  $\sigma_\epsilon/(1+\epsilon)$ -to- $\sigma_\alpha/\alpha$  ratio we obtain is  $\sim 1.0$  before reconstruction and  $\sim 1.5$  after reconstruction which is roughly consistent with the Fisher matrix prediction of  $\sim 1.2$ . Lastly, we note that our  $\sigma_H/H$ -to- $\sigma_{D_A}/D_A$  ratio is  $\sim 2$ , consistent with the predictions of Seo & Eisenstein (2007) and the assumption that went into our Fisher matrix predictions (see Appendix A).

We again test the robustness of our  $\alpha$  and  $\epsilon$  measure-

ments to our fitting model. The results are listed in Table 4. We see that our  $\alpha$  and  $\epsilon$  measurements are always consistent with the results obtained using the fiducial fitting parameters. Our  $\sigma_\alpha$  and  $\sigma_\epsilon$  measurements show  $\sim 10\%$  variations which are consistent with the differences in scatter between the various cases seen in the mocks.

We also test the robustness of our reconstruction technique by varying the input parameters and then re-performing our fits. The  $\alpha$  and  $\epsilon$  values we measure from these tests are also listed in Table 4. Again we see very consistent  $\alpha$ ,  $\epsilon$ ,  $\sigma_\alpha$  and  $\sigma_\epsilon$  values between the various cases. This indicates that our measurements of the acoustic scale and anisotropy are robust against reconstruction parameters.

**Table 4.** DR7 fitting results for various models. The model is given in column 1. The measured  $\alpha$  values are given in column 2 and the measured  $\epsilon$  values are given in column 3. The  $\chi^2/\text{dof}$  is given in column 4.

Model	$\alpha$	$\epsilon$	$\chi^2/\text{dof}$
Redshift Space without Reconstruction			
Fiducial [ $f$ ]	$1.015 \pm 0.044$	$0.007 \pm 0.044$	89.60/90
Fit w/ $(\Sigma_{\perp}, \Sigma_{\parallel}) \rightarrow (8, 8)h^{-1}\text{Mpc}$ .	$1.012 \pm 0.045$	$0.009 \pm 0.042$	89.77/90
Fit w/ $\Sigma_s \rightarrow 0h^{-1}\text{Mpc}$ .	$1.018 \pm 0.040$	$0.007 \pm 0.037$	89.60/90
Fit w/ $A_2(r) = \text{poly}2$ .	$1.018 \pm 0.043$	$0.013 \pm 0.044$	91.42/91
Fit w/ $A_2(r) = \text{poly}4$ .	$1.015 \pm 0.044$	$0.006 \pm 0.045$	89.58/89
Fit w/ $30 < r < 200h^{-1}\text{Mpc}$ range.	$1.018 \pm 0.039$	$0.004 \pm 0.042$	105.03/104
Fit w/ $70 < r < 200h^{-1}\text{Mpc}$ range.	$1.016 \pm 0.050$	$0.008 \pm 0.049$	82.43/76
Fit w/ $50 < r < 150h^{-1}\text{Mpc}$ range.	$1.019 \pm 0.042$	$0.001 \pm 0.046$	47.10/58
Redshift Space with Reconstruction			
Fiducial [ $f$ ]	$1.012 \pm 0.024$	$-0.014 \pm 0.035$	62.53/90
Fit w/ $(\Sigma_{\perp}, \Sigma_{\parallel}) \rightarrow (2, 4)h^{-1}\text{Mpc}$ .	$1.012 \pm 0.025$	$-0.014 \pm 0.036$	62.48/90
Fit w/ $\Sigma_s \rightarrow 0h^{-1}\text{Mpc}$ .	$1.013 \pm 0.021$	$-0.013 \pm 0.027$	61.83/90
Fit w/ $A_2(r) = \text{poly}2$ .	$1.013 \pm 0.025$	$-0.011 \pm 0.036$	65.61/91
Fit w/ $A_2(r) = \text{poly}4$ .	$1.013 \pm 0.025$	$-0.011 \pm 0.036$	61.92/89
Fit w/ $30 < r < 200h^{-1}\text{Mpc}$ range.	$1.014 \pm 0.023$	$-0.013 \pm 0.033$	68.39/104
Fit w/ $70 < r < 200h^{-1}\text{Mpc}$ range.	$1.012 \pm 0.027$	$-0.016 \pm 0.040$	54.50/76
Fit w/ $50 < r < 150h^{-1}\text{Mpc}$ range.	$1.017 \pm 0.023$	$-0.009 \pm 0.033$	31.95/58
Recon. w/ $\beta \rightarrow 0.24$ .	$1.014 \pm 0.024$	$-0.016 \pm 0.034$	68.77/90
Recon. w/ $\beta \rightarrow 0.36$ .	$1.013 \pm 0.024$	$-0.013 \pm 0.035$	67.05/90
Recon. w/ $b \rightarrow 1.8$ .	$1.014 \pm 0.025$	$-0.017 \pm 0.035$	66.75/90
Recon. w/ $b \rightarrow 2.6$ .	$1.015 \pm 0.024$	$-0.012 \pm 0.034$	77.09/90
Recon. w/ Wiener Filter.	$1.012 \pm 0.025$	$-0.014 \pm 0.035$	61.23/90

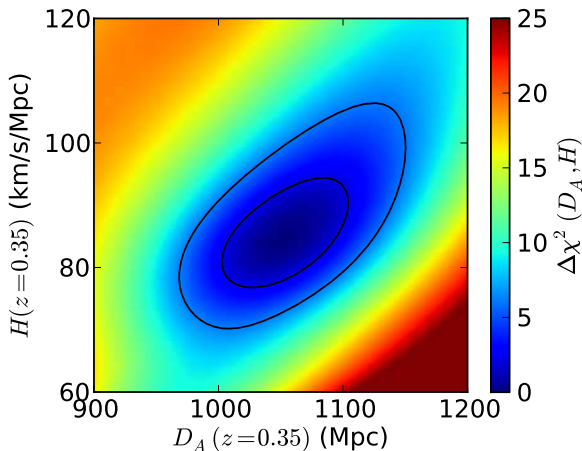


**Figure 17.** The post-reconstruction SDSS DR7  $\Delta\chi^2(D_A, H) = \chi^2(D_A, H) - \chi_{min}^2$  distribution with 1 and  $2\sigma$  contours overplotted. We measure  $D_A(z) = 1050 \pm 38$  Mpc and  $H(z) = 84.4 \pm 7.0$  km/s/Mpc at  $z = 0.35$ . The tilted elliptical contours clearly indicate a correlation between our  $D_A$  and  $H$  measurements. The correlation coefficient is  $\rho_{D_A H} = 0.57$ .

## 6.2 Comparison with Past Works

Three past papers, Gaztañaga, Cabré & Hui (2011), Chuang & Wang (2012a) and Chuang & Wang (2012b), have performed anisotropic BAO analyses using the DR7 LRG sample. Of these, Gaztañaga, Cabré & Hui (2011) found a peak in the clustering along the line-of-sight that they interpret as a detection of the acoustic peak, but Kazin et al. (2010b) show that the peak is consistent with the expected noise.

Chuang & Wang (2012a), hereafter CW12a, measure  $D_A(z = 0.35)$  and  $H(z = 0.35)$  by fitting the 2D correlation function of the LRGs before reconstruction, whereas Chuang & Wang (2012b), hereafter CW12b, fit the monopole and quadrupole. The former measures  $D_A(z = 0.35) = 1048_{-58}^{+60}$  Mpc and  $H(z = 0.35) = 82.1_{-4.9}^{+4.8}$  km/s/Mpc at  $z = 0.35$  while the latter measures  $D_A(z = 0.35) = 1057_{-87}^{+88}$  Mpc and  $H(z = 0.35) = 79.6_{-8.7}^{+8.3}$  km/s/Mpc. These values are all consistent with our pre-reconstruction measurements, however, the magnitudes of the errors are slightly different. Since our treatments of the covariance matrix differ, this is not surprising.

A significant difference between our analysis and that of CW12a and CW12b is that they use a Markov

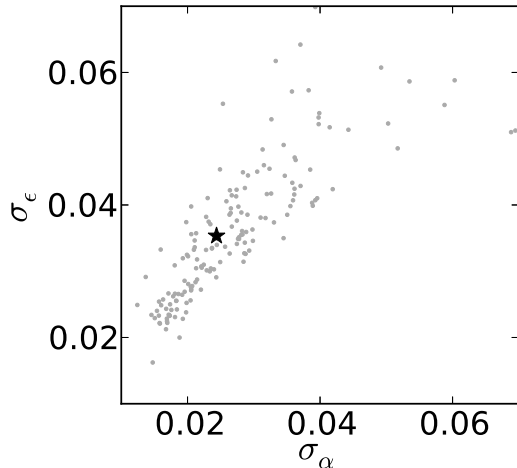


**Figure 18.** Post-reconstruction  $\sigma_\alpha$  versus  $\sigma_\epsilon$  for the mocks with the DR7 point overplotted as the black star. Note that the mock points are identical to Figure 9. We see that our DR7 measurement falls nicely within the locus of mock points. The DR7  $\sigma_\epsilon/(1+\epsilon)$ -to- $\sigma_\alpha/\alpha$  ratio is  $\sim 1.0$  before reconstruction and  $\sim 1.5$  after reconstruction, roughly consistent with the Fisher matrix prediction of  $\sim 1.2$ .

Chain Monte Carlo approach over the parameter space  $\{D_A(z), H(z), \beta, \Omega_m h^2, \Omega_b h^2, n_s, \Sigma_s, \Sigma_{nl}\}$  to derive their  $D_A$  and  $H$  measurements. Both  $\beta$  and  $\Sigma_s$  measure anisotropy due to redshift-space distortions in the broadband correlation function which we do not attempt in our analysis. The method we employ uses the  $A(r)$  term to marginalize out broadband information and focuses only on using the anisotropic information in the BAO. In addition, the FoG model employed by CW12a and CW12b is roughly the square-root of our model. Recall that FoG arises from a perceived change in a galaxy’s cosmological redshift due to its peculiar motion along the line-of-sight. We assume that the peculiar velocity distribution within a halo is exponential and convolve this with the density field directly, thus yielding the power of two in our FoG model for the power spectrum. In the model used by CW12a and CW12b, the galaxy pair-wise velocity is assumed to be exponentially distributed which effectively results in the correlation function being convolved with an exponential. This model is also well motivated as discussed in detail in Hamilton (1998) and Angulo et al. (2008).

Reid & White (2011) has shown that accurately modeling broadband redshift-space distortions in dark matter-only simulations is a challenging theory problem and requires going beyond simple  $\Sigma_s$  and  $\beta$  parameterizations. They demonstrate that neglecting bispectrum and higher order terms from the real to redshift space transformation results in inaccurate models. However, Angulo et al. (2008) have shown that the model used in CW12a and CW12b faithfully describes the clustering of particular populations of galaxies. Further work will be necessary to determine the robustness of such models across galaxy types, especially as the statistical precision of the measurements increase. By comparison, this work attempts to avoid these uncertainties by focusing only on the BAO feature, at the cost of not using all the available information. It is conceivable that any

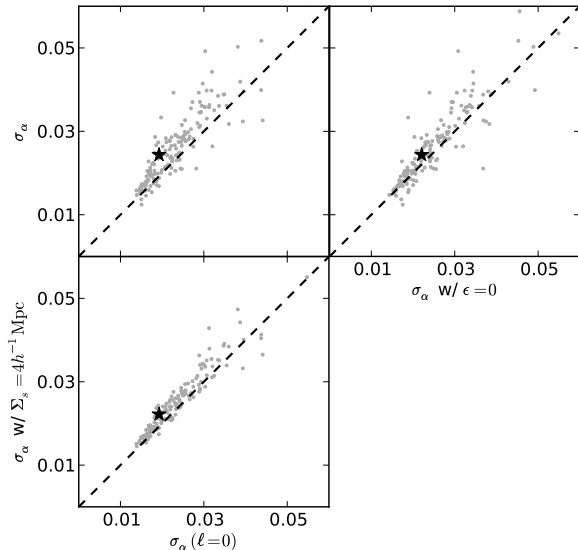


**Figure 19.** The  $\sigma_\alpha$  values measured from the post-reconstruction mocks for various fitting models. The DR7 results are overplotted as the black stars and fall within the locus of mock points. (top left) The  $\sigma_\alpha$  values measured through the full monopole+quadrupole fits versus the monopole-only results of Xu et al. (2012). One can see that the full fits have  $\sigma_\alpha$  that are larger on average. There is also considerable scatter at large  $\sigma_\alpha$  where the acoustic scale is not as well measured. We emphasize however, that these variations in  $\sigma_\alpha$  are incredibly small and do not significantly affect our results. (bottom left)  $\sigma_\alpha$  from monopole+quadrupole fits with  $\Sigma_s = 4h^{-1}\text{Mpc}$  and  $\Sigma_{nl} = 3h^{-1}\text{Mpc}$  versus those from the monopole-only fits with  $\Sigma_s = 0h^{-1}\text{Mpc}$  and  $\Sigma_{nl} = 4h^{-1}\text{Mpc}$ . The degradation in  $\sigma_\alpha$  is obvious and accounts for half the increase in  $\sigma_\alpha$  relative to the monopole-only case. This again suggests that there is some mismatch between our fitting model and the data. (top right)  $\sigma_\alpha$  from full monopole+quadrupole fits including  $\epsilon$  versus those from the monopole+quadrupole fits with  $\epsilon = 0$ . The introduction of  $\epsilon$  appears to cause most of the scatter in  $\sigma_\alpha$  and is responsible for the other half of the  $\sigma_\alpha$  increase relative to the monopole-only case.  $\epsilon$  is known to have some correlation with  $\alpha$  so this is not surprising.

of these differences may give rise to the error discrepancy seen between our results and those of CW12a and CW12b.

Our DR7  $\alpha$  measurements are consistent with the monopole-only measurements of Xu et al. (2012), however, our errorbars on  $\alpha$  are a factor of 1.25 larger both before and after reconstruction. Although this is a very small change in absolute terms, it is still worthy of some investigation. The top left panel of Figure 19 shows the  $\sigma_\alpha$  values we measure for our full monopole+quadrupole fits as described in §3.3 from the post-reconstruction mocks versus the monopole-only results of Xu et al. (2012). The DR7 results are overplotted as the black star. We see that, in general, the mocks have larger  $\sigma_\alpha$  values in our full monopole+quadrupole fits. The scatter at large  $\sigma_\alpha$  where the acoustic scale is not well measured is also significantly bigger. Our DR7  $\sigma_\alpha$  measurement lies within the locus of mock points and hence the increase we see is consistent with the mocks.

Our monopole+quadrupole full fits have several differences relative to the monopole-only fits of Xu et al. (2012). First, the covariance matrix is expanded to include the



**Table 5.** Changes in  $\sigma_\alpha$  relative to the monopole-only fits of Xu et al. (2012) that arise when we introduce new fitting elements. In the first row we introduce the quadrupole fitting with the new combined monopole+quadrupole covariance matrix. The second row introduces our  $\beta$  fitting in addition to the new covariance matrix while the third row introduces changes in  $\Sigma_s$  and  $\Sigma_{nl}$  instead. The fourth row combines the previous two and corresponds to fitting with the fiducial model while forcing  $\epsilon = 0$ . The last row introduces  $\epsilon$  fitting and corresponds to our fiducial model results.

Parameters	Before Recon.		After Recon.	
	$\widetilde{\Delta\sigma_\alpha}$	Qtls	$\widetilde{\Delta\sigma_\alpha}$	Qtls
New $C_{ij}$	0.0007	+0.0014 -0.0015	0.0005	+0.0020 -0.0016
New $C_{ij}$ , adding $\beta$ fit	0.0007	+0.0030 -0.0016	0.0006	+0.0018 -0.0019
New $C_{ij}$ , $\Sigma_s = 4h^{-1}\text{Mpc}$ , new $\Sigma_{nl}$	0.0015	+0.0017 -0.0016	0.0013	+0.0021 -0.0016
New $C_{ij}$ , adding $\beta$ fit, $\Sigma_s = 4h^{-1}\text{Mpc}$ , new $\Sigma_{nl}$ (fiducial model w/ $\epsilon = 0$ )	0.0018	+0.0024 -0.0017	0.0014	+0.0014 -0.0016
New $C_{ij}$ , adding $\beta$ & $\epsilon$ fits, $\Sigma_s = 4h^{-1}\text{Mpc}$ , new $\Sigma_{nl}$ (fiducial model)	0.0036	+0.0040 -0.0044	0.0022	+0.0039 -0.0027

quadrupole-quadrupole and monopole-quadrupole covariances. Second, we introduce  $\beta$  as a fitting parameter. Third, we include FoG (i.e.  $\Sigma_s = 4h^{-1}\text{Mpc}$ ) in our fitting model; Xu et al. (2012) have  $\Sigma_s$  implicitly set to  $0h^{-1}\text{Mpc}$ . Since  $\Sigma_s$  can induce some smearing of the BAO, the  $\Sigma_{nl}$  value we use in the full fits is correspondingly smaller ( $3h^{-1}\text{Mpc}$  versus  $4h^{-1}\text{Mpc}$  in the monopole-only case). In addition, in our pre-reconstruction fitting model, we introduce a non-isotropic  $\Sigma_{nl}$ . To understand which of these steps induces the greatest change in  $\sigma_\alpha$ , we start by fitting the monopole+quadrupole using the new covariance matrix and gradually add in the other changes. Before we describe our results, we again stress that the changes in  $\sigma_\alpha$  we see are very small and require probing some subtleties in our models to understand. Our measurements of  $\alpha$  and  $\sigma_\alpha$  are still reasonably robust against fitting parameters in a single DR7 realization as shown in Tables 2 & 4.

The median changes in  $\sigma_\alpha$  (relative to the monopole-only case) as we add in more elements of the fitting are listed in Table 5 for the pre- and post-reconstruction mocks. The total change between the monopole-only fits and the full monopole+quadrupole fits is listed in the last row of this table. We find that changing the covariance matrix (first row) increases  $\sigma_\alpha$  by a small amount and adding  $\beta$  (second row) does not further degrade the errors. Introducing  $\Sigma_s$  and the accompanying change in  $\Sigma_{nl}$  (third row) appears to be a major contributor to the degradation of  $\sigma_\alpha$ . This increases the median  $\sigma_\alpha$  by about half the total. Combining the  $\beta$  fitting and the changes in  $\Sigma_s$  and  $\Sigma_{nl}$  (fourth row) shows little additional degradation above the previous case. Note that this corresponds to using the fiducial model with  $\epsilon$  fixed at 0. Finally, as mentioned above, the last row adds in  $\epsilon$  fitting and corresponds to the fiducial model. We see that this step causes the other half of the total increase in  $\sigma_\alpha$ . It also introduces a significant amount of scatter in  $\sigma_\alpha$ .

The steps that contribute the most to the  $\sigma_\alpha$  increase are shown in the bottom left and top right panels of Figure 19 for the post-reconstruction case. In the bottom left we have plotted the  $\sigma_\alpha$  values measured from monopole+quadrupole fits with  $\Sigma_s = 4h^{-1}\text{Mpc}$  and  $\Sigma_{nl} = 3h^{-1}\text{Mpc}$  versus those measured from the monopole-only fits with  $\Sigma_s = 0h^{-1}\text{Mpc}$  and  $\Sigma_{nl} = 4h^{-1}\text{Mpc}$ . The offset between the two is obvious and again suggests that our FoG model is not perfectly matched to the data.

The top right panel shows the  $\sigma_\alpha$  values measured from the mocks through the full monopole+quadrupole fits versus

the monopole+quadrupole fits with  $\epsilon$  fixed at 0. In addition to the obvious offset, we also see the appearance of significant scatter.  $\epsilon$  has small but non-zero correlation with  $\alpha$ , implying a slight degeneracy between these 2 parameters. It is not surprising that this extra covariance may increase  $\sigma_\alpha$  and its scatter. Again, this small degradation is not of great concern at our current levels of statistical precision.

## 7 COSMOLOGICAL IMPLICATIONS

In this section we will place our measurement of  $\epsilon$  within the context of current cosmological constraints. To build more intuition for how  $\alpha(z)$  and  $\epsilon(z)$  vary as we change the amount of curvature or the nature of dark energy, we look to Figure 20. The left panel shows  $\alpha$  as a function of redshift for a cosmology that has positive curvature ( $\Omega_K = 0.1$ ), dark energy that is not a cosmological constant ( $w_0 = -0.9$ ) and time-varying dark energy ( $w_a = 0.5$ ). The analogous plot for  $\epsilon$  is shown in the right panel. Here we have again taken the fiducial cosmology to be the flat  $\Lambda\text{CDM}$  cosmology predicted by WMAP7. As we vary the cosmology, we fix  $\Omega_m h^2$  and the distance to the last scattering surface (i.e. the distance to  $z = 1089$ , the redshift of recombination). This guarantees that the sound horizon and the CMB remain approximately unchanged in all the plotted cosmologies.

Recall that if the fiducial cosmology matches the true cosmology of the universe, then we would expect  $\alpha = 1$  and  $\epsilon = 0$ . We see that introducing curvature and altering the nature of dark energy both perturb  $\alpha$  away from 1 the most at low redshift. However, at higher redshift, it becomes increasingly difficult to distinguish between non-cosmological constant models and time-varying dark energy models using measurements of  $\alpha$ . The opposite is true for  $\epsilon$ . We see that the effects of adding curvature or changing the properties of dark energy are most prominent at larger redshifts, peaking at  $z \sim 1$ . This suggests that to exploit the anisotropic BAO signal, we gain more leverage by going to higher  $z$ . However, we also see that even the maximum difference in  $\epsilon$  between the  $w_a = 0.5$  and  $\Omega_K = 0.1$  cosmologies is smaller than our current error on  $\epsilon$  which indicates that we are not able to distinguish between these cosmologies using our DR7 measurement.

Figure 21 shows our DR7 measurement of  $\epsilon$  overplotted on constraints derived from cosmological Markov Chain Monte Carlo (MCMC) sampling. The MCMC method computes the likelihood that a set of input cosmological param-

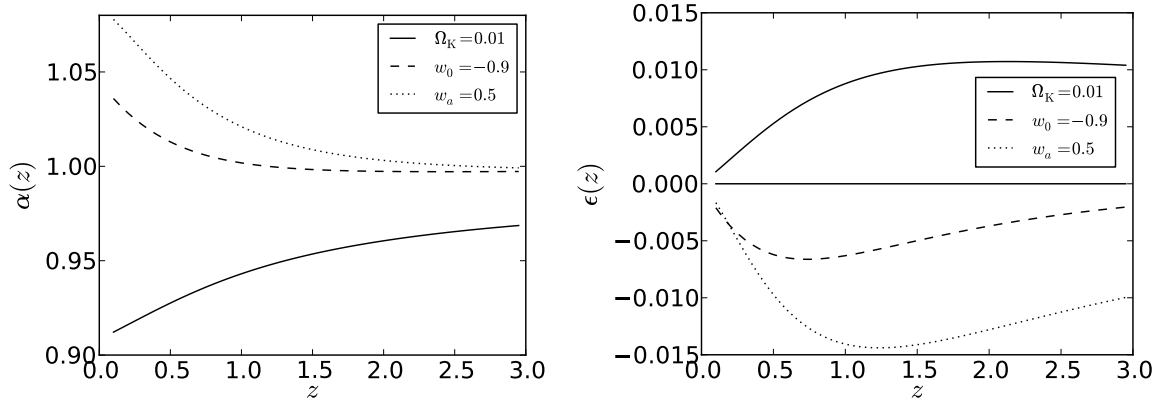


**Figure 20.** The expected variation in  $\alpha(z)$  (left) and  $\epsilon(z)$  (right) as we open up curvature or allow non-cosmological constant or time-varying dark energy. We have taken the fiducial cosmology to be the flat,  $\Lambda$ CDM cosmology predicted by WMAP7 as usual. One can see that curvature and dark energy properties affect  $\alpha$  more at low  $z$ . At high  $z$  it becomes increasingly difficult to distinguish between non-cosmological constant and time-varying dark energy models using measurements of  $\alpha$ . However, we see that  $\epsilon$  is affected by curvature and dark energy the most at higher  $z$ , peaking at  $z \sim 1$ . This suggests that the anisotropic BAO signal is stronger and therefore offers more constraining power at higher redshifts.

eters fits distance measures from Cosmic Microwave Background (CMB) observations at high redshift, and Type Ia supernova (SN) and BAO observations at low redshift. The number of steps in the chain spent exploring a certain region in the cosmological parameter space is proportional to the likelihood of that region representing the true cosmology. Hence, we can infer  $D_A(z)$  and  $H(z)$  at each step in the chain to compute  $\epsilon(z)$  relative to some fiducial cosmology (WMAP7 in our case). At each  $z$ , we can measure the mean and rms of the  $\epsilon$  distribution which can then be compared to our DR7 measurement at  $z = 0.35$ .

The grey regions in Figure 21 are derived from MCMC chains exploring a cosmology which is allowed to have curvature and varying dark energy with equation of state  $w(a) = w_0 + (1-a)w_a$  where  $a$  is the scale factor. Note that this is the most generalized and least-constraining cosmology that is typically tested and is the reference cosmology defined by the Dark Energy Task Force (the DETF cosmology; Albrecht et al. 2006). These chains were computed using CosmoMC, a standard MCMC sampler (Lewis & Bridle 2002). The dark grey and light grey regions correspond to the  $1\sigma$  limits calculated from chains using CMB+BAO data and CMB+BAO+SN data respectively. The CMB data is taken from WMAP7 (Jarosik et al. 2011; Larson et al. 2011) and the SN distance constraints are taken from the Supernova Legacy Survey 3 (SNLS3; Conley et al. 2011).

The BAO distance measure used in the chains is based on our DR7 anisotropic measurements, however, we marginalize over  $\epsilon$  and only use the remaining isotropic or spherically-averaged information encoded in  $\alpha$ . This is equivalent to using  $p(\alpha)$ , the probability distribution for the spherically-averaged distance  $D_V$  to  $z = 0.35$  (plotted in Figure 16), obtained by applying Equation (53) to our measured  $p(\alpha, \epsilon)$ . Figure 21 overplots our DR7  $\epsilon$  measurement on the  $\epsilon$  constraints obtained through our chains. One can see that our DR7 measurement of  $\epsilon$  is consistent with the CMB+BAO and CMB+BAO+SN constraints at  $z = 0.35$ . In the CMB+BAO case, our DR7  $\epsilon$  errorbar falls within the  $\epsilon$  constraints obtained by using the spherically-averaged

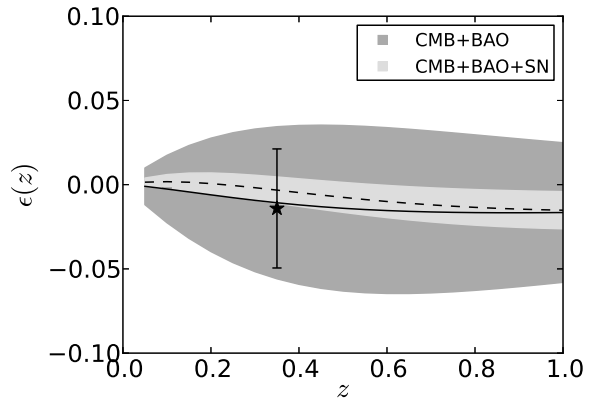


**Figure 21.** Our DR7  $\epsilon$  measurement at  $z = 0.35$  overplotted on the  $1\sigma$  regions predicted by MCMC chains computed via combining CMB+BAO (dark grey) and CMB+BAO+SN (light grey) datasets. The solid black line corresponds to the mean  $\epsilon(z)$  from the CMB+BAO chain and the dashed black line is the analogue for the CMB+BAO+SN chain. Here we have assumed a WMAP7 fiducial cosmology. The plotted chains assumed a DETF cosmology (Albrecht et al. 2006) in which the universe is allowed to be curved and the dark energy equation of state takes on the form  $w(a) = w_0 + (1-a)w_a$ . The CMB data used is taken from WMAP7 (Jarosik et al. 2011; Larson et al. 2011) and the SN distance constraints used are taken from the SNLS3 (Conley et al. 2011). The BAO distance constraints comes from applying Equation (53) to the DR7  $p(\alpha, \epsilon)$  distribution in order to obtain  $p(\alpha)$ , collapsing our 2D constraint into a single constraint on the spherically-averaged distance  $D_V$  to  $z = 0.35$ . This is equivalent to marginalizing over  $\epsilon$ . One can see that our DR7  $\epsilon$  measurement overlaps the regions predicted by our chains very well. In addition, we see that our errorbars on  $\epsilon$  are smaller than the region predicted by using the spherically-averaged constraint  $p(\alpha)$  in the CMB+BAO case. Hence the anisotropic information encoded in our measurement of  $\epsilon$  provides additional constraints on the parameter space of allowed cosmologies.

distance measure. This suggests that the DR7 anisotropic information we measure offers additional constraints on the allowed cosmological parameter space.

The bold text in Table 6 lists results from CosmoMC chains run using our DR7  $\alpha$  and  $\epsilon$  measurements. In the table,  $\Lambda$ CDM refers to a cosmology in which  $\Omega_K$  is allowed to vary (i.e. the universe is allowed to be curved),  $w$ CDM refers to a cosmology in which dark energy is allowed to vary from a cosmological constant and  $\Lambda$ CDM is the DETF cosmology. Here we have combined our full anisotropic BAO measurements at  $z = 0.35$  with observations of the CMB from WMAP7 (Komatsu et al. 2011) and, in the case of the DETF cosmology, supernovae from the SNLS3 (Conley et al. 2011). We compare these with the results from Mehta et al. (2012) (non-bold text in the table) and find consistent measurements and errors for the cosmologies tested. In addition, using the  $\epsilon$ -marginalized  $p(\alpha)$  distribution obtained by applying Equation (53) to  $p(\alpha, \epsilon)$  gives similarly consistent values of the cosmological parameters. However, as expected, the errors can be  $\sim 10 - 20\%$  higher in this case since we are not including the DR7 anisotropic constraints.

Recall that the errors on  $\alpha$  we measure from DR7 are larger than those measured by Xu et al. (2012) and used in Mehta et al. (2012). The fact that our chains produce similar errors on the cosmological parameters implies that we are obtaining some constraint from  $\epsilon$ . Since the fully anisotropic analysis presented here is a more careful treatment of BAO measurements, the similarity in results confirms the validity of past monopole-only BAO analyses. We also note that the redshift of DR7 ( $z = 0.35$ ) is relatively low and as shown in Figure 20, the main constraining power of  $\epsilon$  comes in at larger redshifts. This implies that anisotropic analyses should be more powerful than monopole-only analyses as we go to higher  $z$ .

The future is bright with the SDSS DR9 CMASS sample (Anderson et al. 2012) now in hand. The galaxies in this dataset are denser and more abundant than DR7, and also at higher redshift ( $z = 0.57$ ). Therefore, the DR9 CMASS anisotropic BAO signal should be less noisy and more prominent, implying a much tighter constraint on  $\epsilon$ .

## 8 CONCLUSIONS

The differential clustering along the line-of-sight and transverse directions that arise from assuming the wrong fiducial cosmology can be used to directly constrain the angular diameter distance  $D_A(z)$  and the Hubble parameter  $H(z)$ . This anisotropy can be measured from the BAO signal in the monopole and quadrupole moments of 2-point statistics such as the correlation function studied in this work.

We have presented measurements of the anisotropic BAO signal ( $\epsilon$ ) from the SDSS DR7 LRG sample including density-field reconstruction. We measured  $\alpha = 1.012 \pm 0.024$  and  $\epsilon = -0.014 \pm 0.035$  which translate into  $D_A(z = 0.35) = 1050 \pm 38$  Mpc and  $H(z = 0.35) = 84.4 \pm 7.0$  km/s/Mpc assuming  $r_s = 152.76$  Mpc. Note that these measurements of  $D_A$  and  $H$  are correlated with  $\rho_{D_A H} = 0.57$ . We have demonstrated that the methods for extracting  $\epsilon$  outlined in this paper are robust and applicable to future anisotropic BAO studies.

We have given a detailed account of the theoretical background motivating the origin of the anisotropic signal and a parameter,  $\epsilon$ , for measuring it. An in-depth look at the fitting model and method we use to extract the anisotropic signal is also given. We find that our model parameters have different morphological structures in their derivatives from  $\epsilon$ , although they can still be partially degenerate with each other. These minor degeneracies appear to introduce a small bias in  $\epsilon$  at the 0.2% level, far below our current level of statistical precision.

We apply density field reconstruction and test the robustness of our measured  $\alpha$  and  $\epsilon$  against changes in the reconstruction parameters using 160 LasDamas mock catalogues. We find that reconstruction appears to introduce some anisotropy into the quadrupole, however this is adequately accounted for by our  $A_2(r)$  nuisance parameters. We then perform the same robustness checks on our fitting model using the mock catalogues. Similar tests were also performed on the DR7 data returning consistently robust results. We demonstrate that  $\alpha$  and  $\epsilon$  have near-Gaussian posteriors. Hence estimating their errors ( $\sigma_\alpha$  and  $\sigma_\epsilon$ ) as the second moments of their respective probability distributions is reasonable. The  $\sigma_\alpha$ ,  $\sigma_\epsilon$  and  $\rho_{\alpha\epsilon}$  values obtained from the mocks and the DR7 data are mostly consistent with Fisher matrix predictions.

We find that in the mocks and the DR7 data, our  $\alpha$  error estimates are slightly larger than those obtained when only the monopole is fit. This small increase does not detract significantly from the overall robustness of our measurements which we verify as discussed above. About half of this increase is a result of including an FoG model in our full monopole+quadrupole fits while the other half arises from fitting for  $\epsilon$ . This first point suggests that our FoG model does not match the data perfectly and may induce slight biases into our measurements. Given the non-zero covariance between  $\epsilon$  and  $\alpha$  the second point is not surprising. The behaviour of DR7 falls completely within the locus of mock points and is therefore not unusual.

Our DR7 measurements of  $D_A$  and  $H$  before reconstruction are consistent with those obtained by Chuang & Wang (2012a) and Chuang & Wang (2012b) using the same dataset. The errors we measure, however, differ slightly due to differences in our analysis techniques. The errors on  $\alpha$  and  $\epsilon$  we measure from the DR7 data are consistent with the scatter from the mocks. In addition, our  $\sigma_\epsilon/(1 + \epsilon)$ -to- $\sigma_\alpha/\alpha$  ratio agrees reasonably well with Fisher matrix predictions and our  $\sigma_H/H$ -to- $\sigma_{D_A}/D_A$  ratio is  $\sim 2$  and in good agreement with the predictions of Seo & Eisenstein (2007).

Our post-reconstruction DR7  $\epsilon$  measurement agrees well with the predictions from current datasets. Comparing the cosmological parameters we obtain using our  $\alpha$  and  $\epsilon$  measurements with the monopole-only measurements in Mehta et al. (2012) yields consistent values and errors. This suggests that although our errors on  $\alpha$  are larger than the monopole-only case, the  $\epsilon$  measurement is providing some additional constraint on the cosmological parameters. The validity of previous monopole-only analyses is also confirmed by the similarity between those cosmological results and the ones obtained here through a more careful, fully-anisotropic analysis of the BAO.

We find that the anisotropic signal is stronger at higher redshifts which suggests that its constraining power will be

**Table 6.** Cosmological parameters measured from CosmoMC chains. The first line listed for each cosmology is the DR7 monopole-only result from Mehta et al. (2012). The second (bold) line is derived from our DR7  $\alpha$  and  $\epsilon$  measurements.

Cosmology	Datasets	$\Omega_m h^2$	$\Omega_m$	$H_0$	$\Omega_K$	$w_0$	$w_a$
$\Lambda$ CDM	CMB+BAO	0.1333(53)	0.278(15)	69.3(16)	-0.004(5)	–	–
		<b>0.1342(50)</b>	<b>0.285(16)</b>	<b>68.7(18)</b>	<b>-0.003(5)</b>	–	–
$w$ CDM	CMB+BAO	0.1349(57)	0.285(25)	69.0(39)	–	-0.97(17)	–
		<b>0.1347(57)</b>	<b>0.289(26)</b>	<b>68.4(38)</b>	–	<b>-0.95(17)</b>	–
$ow_0w_a$ CDM	CMB+BAO+SN	0.1346(53)	0.276(15)	69.9(19)	-0.010(7)	-0.90(16)	-1.30(99)
		<b>0.1352(52)</b>	<b>0.280(17)</b>	<b>69.6(21)</b>	<b>-0.010(7)</b>	<b>-0.90(16)</b>	<b>-1.32(100)</b>

come more apparent at higher  $z$ . The recently obtained SDSS DR9 CMASS dataset has a higher number density than the DR7 LRG sample, contains more galaxies and is at higher redshift ( $z = 0.57$ ). The basic theory and methodology presented in this work should serve as a foundation for obtaining a much better detection of  $\epsilon$ , and subsequently  $D_A$ ,  $H$  and other cosmological parameters from CMASS.

## 9 ACKNOWLEDGMENTS

Funding for the Sloan Digital Sky Survey (SDSS) and SDSS-II has been provided by the Alfred P. Sloan Foundation, the Participating Institutions, the National Science Foundation, the U.S. Department of Energy, the National Aeronautics and Space Administration, the Japanese Monbukagakusho, the Max Planck Society and the Higher Education Funding Council for England. The SDSS website is <http://www.sdss.org/>.

The SDSS is managed by the Astrophysical Research Consortium (ARC) for the Participating Institutions. The Participating Institutions are the American Museum of Natural History, Astrophysical Institute Potsdam, University of Basel, University of Chicago, Drexel University, Fermilab, the Institute for Advanced Study, the Japan Participation Group, the Johns Hopkins University, the Joint Institute for Nuclear Astrophysics, the Kavli Institute for Particle Astrophysics and Cosmology, the Korean Scientist Group, the Chinese Academy of Sciences (LAMOST), Los Alamos National Laboratory, the Max-Planck-Institute for Astronomy (MPIA), New Mexico State University, Ohio State University, University of Pittsburgh, University of Portsmouth, Princeton University, the United States Naval Observatory and the University of Washington.

We thank the LasDamas collaboration for making their galaxy mock catalogs public. XX thanks Kushal Mehta for useful conversations. XX and DJE were supported by NSF grant AST-0707725 and NASA grant NNX07AH11G. NP and AJC are partially supported by NASA grant NNX11AF43G. This work was supported in part by the facilities and staff of the Yale University Faculty of Arts and Sciences High Performance Computing Center.

## REFERENCES

- Abazajian, K. N., et al., 2009, ApJS, 182, 543  
 Abdalla, F. B., & Rawlings, S., 2005, MNRAS, 360, 27  
 Albrecht, A., et al., 2006, arXiv:astro-ph/0609591v1  
 Alcock, C., & Paczynski, B., 1979, Nature, 281, 358  
 Amendola, L., Quercellini, C., Giallongo, E., 2005, MNRAS, 357, 429  
 Anderson, L., et al. 2012, MNRAS, submitted  
 Angulo, R., et al., 2005, MNRAS, 362, L25  
 Angulo, R., et al., 2008, MNRAS, 383, 755  
 Beutler, F., et al., 2011, MNRAS, 416, 3017  
 Blake, C., & Glazebrook, K., 2003, ApJ, 594, 665  
 Blake, C., et al., 2011, MNRAS, 418, 1707  
 Blake, C., et al., 2011, MNRAS, 418, 1725  
 Bond, J. R., & Efstathiou, G., 1984, ApJ, 594, 665  
 Carroll, S. M., Press, W. H., & Turner, E. L. 1992, ARA&A, 30, 499  
 Chuang, C.-H., & Wang, Y., 2012, MNRAS, 426, 226  
 Chuang, C.-H., & Wang, Y., 2012, arXiv:1205.5573  
 Cole, S., et al., 2005, MNRAS, 362, 505  
 Conley, A., et al., 2011, ApJS, 192, 1  
 Crocce, M., & Scoccimarro, R., 2008, Phys. Rev. D, 77, 023533  
 Dolney, D., Jain, B., & Takada, M., 2006, MNRAS, 366, 884  
 Eisenstein, D. J., & Hu, W., 1998, ApJ, 496, 605  
 Eisenstein, D. J., Hu, W., Tegmark, M., 1998, ApJL, 504, L57  
 Eisenstein, D. J., et al., 2001, AJ, 122, 2267  
 Eisenstein, D. J., 2003, in ASP Conference Series, Vol. 280, Next Generation Wide Field Multi-Object Spectroscopy, ed. M.J.I. Brown & A. Dey (ASP: San Francisco) pp. 35-43  
 Eisenstein, D. J., et al., 2005, ApJ, 633, 560  
 Eisenstein, D. J., Seo, H.-J., & White, M., 2007, ApJ, 664, 660  
 Eisenstein, D. J., Seo, H.-J., Sirko, E., & Spergel, D. N., 2007, ApJ, 664, 675  
 Feldman, H. A., Kaiser, N., & Peacock, J. A., 1994, ApJ, 426, 23  
 Fisher, K. B., Davis, M., Strauss, M. A., Yahil, A., Huchra, J. P., 1994, MNRAS, 267, 927  
 Fukugita, M., et al., 1996, AJ, 111, 1748  
 Gaztañaga, E., Cabré, A., & Hui, L., 2011, MNRAS, 399, 1663  
 Glazebrook, K., & Blake, C., 2005, ApJ, 631, 1  
 Gunn, J. E., et al., 1998, AJ, 116, 3040  
 Gunn, J. E., et al., 2006, AJ, 131, 2332  
 Guzik, J., Bernstein, G., & Smith, R. E., 2007, MNRAS, 375, 1329  
 Hamilton, A. J. S., 1998, in Astrophysics and Space Science Library, Vol. 231, The Evolving Universe, ed. D. Hamilton pp. 185

Hoffman, Y., & Ribak, E., 1991, ApJ, 380, L5  
 Hogg, D. W., Finkbeiner, D. P., Schlegel, D. J., & Gunn, J. E., 2001, AJ, 122, 2129  
 Holtzman, J. A., 1989, ApJS, 71, 1  
 Hu, W., & Haiman, Z., 2003, Phys. Rev. D, 68, 063004  
 Hu, W., & Sugiyama, N., 1996, ApJ, 471, 542  
 Hu, W., & White, M., 1996, ApJ, 471, 30  
 Huff, E., et al., 2007, Astroparticle Physics, 26, 351  
 Hütsi, G., 2006, A&A, 449, 891  
 Ivezić, Ž., et al., 2004, Astronomische Nachrichten, 325, 583  
 Jarosik, N., et al., 2011, ApJS, 192, 14  
 Jeong, D., & Komatsu, E., 2006, ApJ, 651, 619  
 Kaiser, N., 1987, MNRAS, 227, 1  
 Kazin, E., et al., 2010, ApJ, 710, 1444  
 Kazin, E., et al., 2010, ApJ, 719, 1032  
 Kazin, E., Sánchez, A. G., Blanton, M. R. 2012, MNRAS, 419, 3223  
 Komatsu, E., et al., 2011, ApJS, 192, 18  
 Landy, S. D., & Szalay, A. S., 1993, ApJ, 412, 64  
 Larson, D., et al., 2011, ApJS, 192, 16  
 Lewis, A., & Bridle, S. 2002, Phys. Rev. D, 66, 103511  
 Linder, E. V., 2003, Phys. Rev. D, 68, 083504  
 Linder, E. V., 2005, Phys. Rev. D, 72, 043529  
 Ma, Z., 2007, ApJ, 665, 887  
 Matsubara, T., 2004, ApJ, 615, 573  
 McBride, C., et al., 2012, in prep  
 Meiksin, A., White, M., & Peacock, J. A., 1999, MNRAS, 304, 851  
 Mehta, K., et al., 2011, ApJ, 734, 94  
 Mehta, K., et al., 2012, MNRAS, accepted  
 Noh, Y., White, M., & Padmanabhan, N., 2009, Phys. Rev. D, 80, 123501  
 Nusser, A., & Davis, M., 1994, ApJ, 421, L1  
 Okumura, T., et al., 2008, ApJ, 676, 889  
 Padmanabhan, N., et al., 2008, ApJ, 674, 1217  
 Padmanabhan, N., & White, M. 2008, Phys. Rev. D, 77, 123540  
 Padmanabhan, N., & White, M., 2009, Phys. Rev. D, 80, 063508  
 Padmanabhan, N., White, M., & Cohn, J. D., 2009, Phys. Rev. D, 79, 063523  
 Padmanabhan, N., et al., 2012, MNRAS, submitted  
 Park, C., Vogeley M. S., Geller M. J., Huchra J. P., 1994, ApJ, 431, 569  
 Peebles, P. J. E., & Yu, J. T., 1970, ApJ, 162, 815  
 Percival, W. J., et al., 2007, MNRAS, 381, 1053  
 Percival, W. J., et al., 2010, MNRAS, 401, 2148  
 Perlmutter S., et al., 1999, ApJ, 517, 565  
 Pier, J. R., et al., 2003, AJ, 125, 1559  
 Reid, B. A., & White, M., 2011, MNRAS, 417, 1913  
 Riess, A. G., et al., 1998, AJ, 116, 1009  
 Sanchez, A. G., Baugh, C. M., Angulo, R., 2008, 390, 1470  
 Seo, H.-J., & Eisenstein, D. J., 2003, ApJ, 598, 720  
 Seo, H.-J., & Eisenstein, D. J., 2005, ApJ, 633, 575  
 Seo, H.-J., & Eisenstein, D. J., 2007, ApJ, 665, 14  
 Seo, H.-J., Siegel, E. R., Eisenstein, D. J., White, M., 2008, ApJ, 686, 13  
 Seo, H.-J., et al., 2010, ApJ, 720, 1650  
 Smith, J. A., 2002, AJ, 123, 2121  
 Smith, R. E., Scoccimarro, R., Sheth, R. K., 2008, Phys. Rev. D, 77, 043525  
 Strauss, M. A., 2002, AJ, 124, 1810

Sunyaev, R. A., & Zeldovich, Y. B., 1970, Ap&SS, 7, 3  
 Takahashi, R., et al., 2009, ApJ, 700, 479  
 Taruya, A., Saito, S., & Nishimichi, T., 2012, Phys. Rev. D, 83, 103527  
 Tegmark, M., et al., 2006, Phys. Rev. D, 74, 123507  
 Tucker, D. L., et al., 2006, Astronomische Nachrichten, 327, 821  
 Xu, X., et al., 2012, MNRAS, accepted  
 York, D. G., et al., 2000, AJ, 120, 1579  
 Zaroubi, S., Hoffman, Y., Fisher, K. B., & Lahav, O., 1995, ApJ, 449, 446

## APPENDIX A: FISHER MATRIX PREDICTIONS

Using a Fisher matrix formalism, it is possible to derive theoretical predictions for and expected correlations between the variances and covariances of  $\alpha$ ,  $\epsilon$ ,  $D_A$  and  $H$ . The values derived here are utilized in the text as sanity checks for the values we measure.

We begin with the matrix equation

$$\begin{pmatrix} \sigma_\alpha^2 & \sigma_{\alpha\epsilon} \\ \sigma_{\alpha\epsilon} & \sigma_\epsilon^2 \end{pmatrix} = \begin{pmatrix} \frac{\partial\alpha}{\partial D_A} & \frac{\partial\alpha}{\partial H} \\ \frac{\partial\epsilon}{\partial D_A} & \frac{\partial\epsilon}{\partial H} \end{pmatrix} \begin{pmatrix} \sigma_{D_A}^2 & \sigma_{D_A H} \\ \sigma_{D_A H} & \sigma_H^2 \end{pmatrix} \begin{pmatrix} \frac{\partial\alpha}{\partial D_A} & \frac{\partial\alpha}{\partial H} \\ \frac{\partial\epsilon}{\partial D_A} & \frac{\partial\epsilon}{\partial H} \end{pmatrix}^T. \quad (\text{A1})$$

Note that this is essentially the inverse process to Equation (7). Expanding we get

$$\sigma_\alpha^2 = \sigma_{D_A}^2 \left( \frac{\partial\alpha}{\partial D_A} \right)^2 + \sigma_H^2 \left( \frac{\partial\alpha}{\partial H} \right)^2 + 2\sigma_{D_A H} \frac{\partial\alpha}{\partial D_A} \frac{\partial\alpha}{\partial H} \quad (\text{A2})$$

$$\sigma_\epsilon^2 = \sigma_{D_A}^2 \left( \frac{\partial\epsilon}{\partial D_A} \right)^2 + \sigma_H^2 \left( \frac{\partial\epsilon}{\partial H} \right)^2 + 2\sigma_{D_A H} \frac{\partial\epsilon}{\partial D_A} \frac{\partial\epsilon}{\partial H}. \quad (\text{A3})$$

$$\begin{aligned} \sigma_{\alpha\epsilon} &= \sigma_{D_A}^2 \frac{\partial\alpha}{\partial D_A} \frac{\partial\epsilon}{\partial D_A} + \sigma_{D_A H} \left( \frac{\partial\alpha}{\partial H} \frac{\partial\epsilon}{\partial D_A} + \frac{\partial\alpha}{\partial D_A} \frac{\partial\epsilon}{\partial H} \right) \\ &\quad + \sigma_H^2 \frac{\partial\alpha}{\partial H} \frac{\partial\epsilon}{\partial H} \end{aligned} \quad (\text{A4})$$

Plugging in the relevant derivatives from Equations (3) & (4) we get

$$\frac{\sigma_\alpha^2}{\alpha^2} = \frac{4}{9}\sigma_{\log D_A}^2 + \frac{1}{9}\sigma_{\log H}^2 - \frac{4}{9} \left( \frac{\sigma_{D_A H}}{D_A H} \right) \quad (\text{A5})$$

$$\frac{\sigma_\epsilon^2}{(1+\epsilon)^2} = \frac{1}{9}\sigma_{\log D_A}^2 + \frac{1}{9}\sigma_{\log H}^2 + \frac{2}{9} \left( \frac{\sigma_{D_A H}}{D_A H} \right) \quad (\text{A6})$$

$$\frac{\sigma_{\alpha\epsilon}}{\alpha(1+\epsilon)} = -\frac{2}{9}\sigma_{\log D_A}^2 + \frac{1}{9}\sigma_{\log H}^2 - \frac{1}{9} \left( \frac{\sigma_{D_A H}}{D_A H} \right) \quad (\text{A7})$$

where  $\sigma_{\log y}^2 = \frac{\sigma_y^2}{y^2}$ .

The correlation coefficient between  $D_A$  and  $H$  is  $\rho_{D_A H} = \sigma_{D_A H} / \sigma_{D_A} \sigma_H$ . If we write  $f = \sigma_{\log H} / \sigma_{\log D_A}$ , then we have

$$\frac{\sigma_\alpha^2}{\alpha^2} = \frac{1}{9}\sigma_{\log D_A}^2 (4 + f^2 - 4\rho_{D_A H} f) \quad (\text{A8})$$

$$\frac{\sigma_\epsilon^2}{(1+\epsilon)^2} = \frac{1}{9}\sigma_{\log D_A}^2 (1 + f^2 + 2\rho_{D_A H} f) \quad (\text{A9})$$

$$\frac{\sigma_{\alpha\epsilon}}{\alpha(1+\epsilon)} = \frac{1}{9}\sigma_{\log D_A}^2 (-2 + f^2 - \rho_{D_A H} f). \quad (\text{A10})$$

Note that  $f$  is just the ratio of  $\sigma_H/H$ -to- $\sigma_{D_A}/D_A$  which is typically  $\sim 2$  (Seo & Eisenstein 2007). The correlation coefficient  $\rho_{D_A H}$  is predicted to be  $\sim 0.4$ . Hence, we have

$$\frac{\sigma_\alpha}{\alpha} = \sigma_{\log \alpha} = 0.73\sigma_{\log D_A} \quad (\text{A11})$$

$$\frac{\sigma_\epsilon}{1+\epsilon} = \sigma_{\log(1+\epsilon)} = 0.86\sigma_{\log D_A}, \quad (\text{A12})$$

which implies the ratio

$$\frac{\sigma_\epsilon}{1+\epsilon} - \frac{\sigma_\alpha}{\alpha} \sim 1.2. \quad (\text{A13})$$

The correlation coefficient between  $\alpha$  and  $\epsilon$  is

$$\rho_{\alpha\epsilon} = \frac{\sigma_{\alpha\epsilon}}{\sigma_\alpha\sigma_\epsilon} \quad (\text{A14})$$

$$= \frac{\alpha}{\sigma_\alpha} \frac{(1+\epsilon)}{\sigma_\epsilon} \left( \frac{1}{9}\sigma_{\log D_A}^2 \right) (-2 + f^2 - \rho_{D_A H} f). \quad (\text{A15})$$

Using Equations (A11) & (A12) and plugging in the assumed values of  $f$  and  $\rho_{D_A H}$  gives

$$\rho_{\alpha\epsilon} \sim 0.21. \quad (\text{A16})$$